

The climatic significance of Late Ordovician-early Silurian black

Article

Published Version

Pohl, A., Donnadieu, Y., Le Hir, G. L. and Ferreira, D. (2017) The climatic significance of Late Ordovician-early Silurian black. *Paleoceanography*, 32 (4). pp. 397-423. ISSN 0883-8305 doi: <https://doi.org/10.1002/2016PA003064> Available at <https://centaur.reading.ac.uk/69975/>

It is advisable to refer to the publisher's version if you intend to cite from the work. See [Guidance on citing](#).

To link to this article DOI: <http://dx.doi.org/10.1002/2016PA003064>

Publisher: American Geophysical Union

All outputs in CentAUR are protected by Intellectual Property Rights law, including copyright law. Copyright and IPR is retained by the creators or other copyright holders. Terms and conditions for use of this material are defined in the [End User Agreement](#).

www.reading.ac.uk/centaur

CentAUR

Central Archive at the University of Reading

Reading's research outputs online

RESEARCH ARTICLE

10.1002/2016PA003064

Key Points:

- Up-to-date ocean general circulation model with biogeochemical capabilities (MITgcm)
- Investigating the mechanisms responsible for the burial of organic carbon throughout the Ordovician-Silurian boundary
- Simulations suggest a global ocean oxygenation event during the latest Ordovician Hirnantian

Supporting Information:

- Supporting Information S1

Correspondence to:

A. Pohl,
pohl.alexandre@gmail.com

Citation:

Pohl, A., Y. Donnadieu, G. Le Hir, and D. Ferreira (2017), The climatic significance of Late Ordovician-early Silurian black shales, *Paleoceanography*, 32, 397–423, doi:10.1002/2016PA003064.

Received 29 NOV 2016

Accepted 30 MAR 2017

Accepted article online 13 APR 2017

Published online 20 APR 2017

The climatic significance of Late Ordovician-early Silurian black shales

A. Pohl¹, Y. Donnadieu^{1,2}, G. Le Hir³, and D. Ferreira⁴
¹Laboratoire des Sciences du Climat et de l'Environnement, LSCE/IPSL, CEA-CNRS-UVSQ, Université Paris-Saclay, Gif-sur-Yvette, France, ²Aix Marseille Univ, CNRS, IRD, Coll France, CEREGE, Aix-en-Provence, France, ³Institut de Physique du Globe de Paris, Université Paris7-Denis Diderot, Paris, France, ⁴Department of Meteorology, University of Reading, Reading, United Kingdom

Abstract The Ordovician-Silurian transition (~455–430 Ma) is characterized by repeated climatic perturbations, concomitant with major changes in the global oceanic redox state best exemplified by the periodic deposition of black shales. The relationship between the climatic evolution and the oceanic redox cycles, however, remains largely debated. Here using an ocean-atmosphere general circulation model accounting for ocean biogeochemistry (MITgcm), we investigate the mechanisms responsible for the burial of organic carbon immediately before, during, and right after the latest Ordovician Hirnantian (445–444 Ma) glacial peak. Our results are compared with recent sedimentological and geochemical data. We show that the late Katian time slice (~445 Ma), typified by the deposition of black shales at tropical latitudes, represents an unperturbed oceanic state, with regional organic carbon burial driven by the surface primary productivity. During the Hirnantian, our experiments predict a global oxygenation event, in agreement with the disappearance of the black shales in the sedimentary record. This suggests that deep-water burial of organic matter may not be a tenable triggering factor for the positive carbon excursion reported at that time. Our simulations indicate that the perturbation of the ocean circulation induced by the release of freshwater, in the context of the post-Hirnantian deglaciation, does not sustain over sufficiently long geological periods to cause the Rhuddanian (~444 Ma) oceanic anoxic event. Input of nutrients to the ocean, through increased continental weathering and the leaching of newly exposed glaciogenic sediments, may instead constitute the dominant control on the spread of anoxia in the early Silurian.

1. Introduction

For more than 25 million years (~455–430 Ma), the Late Ordovician-early Silurian underwent periodic episodes of massive organic matter burial, as testified by the abundant black shale record [Cramer and Saltzman, 2007a; Page et al., 2007; Armstrong et al., 2009; Le Heron et al., 2009, 2013; Melchin et al., 2013]. These sedimentary rocks, which include a variety of dark-colored, fine-grained organic-rich lithologies [Arthur, 1979; Trabucho-Alexandre et al., 2012], represent perennial organic carbon burial and sequestration in the oceanic sediments under oxygen-depleted depositional settings. Given the amplitude of these events, some authors [Page et al., 2007; Melchin et al., 2013] propose that they may have been comparable to the widely documented Mesozoic Oceanic Anoxic Events (OAEs) [Schlanger and Jenkyns, 2007; Jenkyns, 2010], although the significantly longer duration of the early Paleozoic OAEs remains difficult to explain (2–3 Myr at least [see Page et al., 2007; Melchin et al., 2013] compared to 600 kyr to 900 kyr for the Cretaceous OAE2 [see Sageman et al., 2006]) and the concomitant deposition of anoxic sediments in the deep ocean debated due to the nonpreservation of pre-Mesozoic ocean bottom sediments.

Despite a comprehensive analysis of combined sedimentological and geochemical data [e.g., Finney et al., 1999; Brenchley et al., 2003; Kump et al., 1999; Trotter et al., 2008; Hammarlund et al., 2012; Melchin et al., 2013], major uncertainties persist about the physical mechanisms that drove the Ordovician-Silurian oxic-anoxic cycles and associated periods of black shale deposition, thus hampering our overall understanding of the coupled Early Paleozoic climate changes and faunal turnovers [Harper et al., 2013a; Trotter et al., 2016]. The relationships between global climate and oceanic redox conditions, in particular, remain largely debated.

Several conceptual models of oceanic cycles were proposed in the past to explain the changes in lithology, biology, and carbon isotope stratigraphy during the early Silurian [Jeppsson, 1990; Bickert et al., 1997; Cramer and Saltzman, 2005]. The seminal model of Jeppsson [1990], in particular, suggests the alternation between two oceanic states. Black shales form in both of these climatic modes, but the locus of organic burial differs. *Primo* (P) episodes correspond to cold periods. The ocean bottom is intensively ventilated by cold, oxygenated water masses originating from the zones of deep convection situated at polar latitudes. As a consequence the deep ocean is devoid of black shales. At tropical latitudes, the weathering of the extended Ordovician shelf platforms exposed during the sea level lowstand promotes the delivery of nutrients to the ocean, fueling the primary productivity and inducing the deposition of black shales on the shelf. Conversely, the warmer climate prevailing during the *Secundo* (S) episodes promotes the stratification of the ocean. The ventilation of the ocean interior is reduced. The ocean bottom is depleted in dissolved oxygen and organic carbon is buried at depth. At low latitudes, arid conditions prevail. The flux of detrital sediments—and thus nutrients—to the ocean is reduced and the shelf platforms experience extensive reef growth.

The P-S model stimulated vigorous scientific discussion [Cramer and Saltzman, 2005, 2007a, 2007b; Loydell, 2007, 2008; Trotter et al., 2016; Munnecke et al., 2010]. Nevertheless, several published studies suggest that the proposed alternation between P and S episodes does not satisfactorily capture the lithological and geochemical changes documented in the sedimentary record [Kaljo et al., 2003; Johnson, 2006; Trotter et al., 2016]. In addition, the previous conceptual models do not permit any spatialized investigation of the redox state of the ocean. Above all, they are not grounded in physical paleoceanography, which remains highly speculative in the Early Paleozoic [Servais et al., 2014].

Here we apply an up-to-date ocean general circulation model to study the coupling between climate and ocean biogeochemistry in the Early Paleozoic. Building on the comprehensive Late Ordovician-early Silurian black shale occurrence compilation of Melchin et al. [2013], we investigate geological events able to explain the deposition of black shales and propose driving mechanisms for the redox changes reported immediately before, during, and right after the latest Ordovician Hirnantian, from the late Katian to early Silurian Rhuddanian. This time interval includes the Hirnantian glacial maximum [Denis et al., 2007; Ghienne et al., 2007; Loi et al., 2010] and associated mass extinction event [Sheehan, 2001; Rasmussen and Harper, 2011; Harper et al., 2013b, 2013a] and ultimately constitutes an outstanding window into the coupled climatic, paleoceanographic, and biotic perturbations reported for the remainder of the Early Paleozoic Ice Age [Page et al., 2007; Trotter et al., 2016; Vandenbroucke et al., 2015].

Following a description of our experimental setup (section 2), we run our model under a large range of external forcing levels in order to simulate the various climatic conditions reported throughout the studied period of time (section 3). Then, we use these climatic results to investigate the mechanisms driving the patterns of marine biogeochemistry reported by Melchin et al. [2013] in each of their three studied time slices: (i) the late Katian (section 4); (ii) the mid-Hirnantian (section 5); and (iii) the early Silurian Rhuddanian (section 6). In section 7, we discuss the limitations and simplifications associated with our modeling setup and identify future research targets. Finally, we summarize our key findings (section 8).

2. Methods

2.1. Model Description

2.1.1. Ocean, Sea Ice, Atmosphere, and Land

We use a global ocean-atmosphere coupled setup of the MITgcm. Isomorphisms between the equations that govern the atmosphere and the ocean are exploited to allow a single hydrodynamical core to simulate both fluids [Marshall et al., 2004]. The oceanic and the atmospheric components use the same horizontal model grid, greatly simplifying their coupling. We adopt the conformally expanded spherical cube [Adcroft et al., 2004], with 32×32 points per face (CS32)—providing a mean equatorial resolution of $2.8^\circ \times 2.8^\circ$. The cubed sphere provides a relatively even grid spacing throughout the domain and avoids polar singularities, thus allowing accurate simulation of the polar regions. This is especially appropriate to investigate the ocean circulation during the Ordovician, when the Northern Hemisphere was 95% oceanic with no continental masses present beyond the midlatitudes. The oceanic component of the model is a state-of-the-art ocean general circulation model (OGCM) rooted in the incompressible, Boussinesq form of the Navier-Stokes equations [Marshall et al., 1997a, 1997b]. Here we use an hydrostatic, implicit free-surface, partial step topography [Adcroft et al., 1997] formulation of the model to simulate the global ocean domain. Twenty-eight layers are defined vertically, the thickness of which gradually increases from 10 m at the ocean surface to 1300 m at

the bottom, with 18 levels defining the upper 1000 m of the water column. Effects of mesoscale eddies are parametrized as an advective process [Gent and McWilliams, 1990] and an isopycnal diffusion [Redi, 1982]. The nonlocal K-Profile Parameterization (KPP) scheme of Large *et al.* [1994] accounts for vertical mixing processes in the ocean's surface boundary layer and the interior. Sea ice is simulated using a thermodynamic sea ice model based on the three-layer enthalpy-conserving scheme of Winton [2000]. Sea ice forms when the ocean temperature falls below the salinity dependent freezing point. The physics of the atmospheric component is based on SPEEDY (Simplified Parametrizations, primitiveE-Quation DYnamics) [Molteni, 2003]. The latter comprises a four-band longwave radiation scheme (one for the atmospheric "window," a CO₂ band with transmissivity tuned to the present-day atmospheric partial pressure of CO₂ (pCO₂) and the other two bands for the spectral regions of absorption by water vapor), a parametrization of moist convection, diagnostic clouds, and a boundary layer scheme. In the vertical dimension, SPEEDY uses five levels. The top and bottom layers respectively represent the stratosphere and the planetary boundary layer. The layers in between account for the free troposphere. SPEEDY has been shown to require at least 1 order of magnitude less computation time than contemporary state-of-the-art atmospheric GCMs, while providing realistic climate results [Molteni, 2003]. Our configuration of the MITgcm also includes a simple, two-layer land model. No explicit river model is included: the amount of water that exceeds the field capacity of the soil in a given grid point is directly transferred to the ocean following a prescribed mapping. No flux corrections are applied in any of our experiments. The resulting coupled model can be integrated for ~100 years in 1 day of dedicated computer time. Relatively similar configurations of the MITgcm were used in the past [Marshall *et al.*, 2007; Enderton and Marshall, 2009; Ferreira *et al.*, 2010, 2011; Brunetti *et al.*, 2015], including for paleoceanographic purposes [Brunetti *et al.*, 2015]. A comprehensive description of the coupled model is provided by Enderton [2009].

2.1.2. Marine Biogeochemistry

The biogeochemistry model included in the present configuration of the MITgcm explicitly accounts for oxygen concentration and primary productivity in the ocean. Following Michaelis-Menten kinetics, and similar to McKinley *et al.* [2004], the net marine primary productivity (NPP) is computed as a function of available photosynthetically active radiation (PAR) and phosphate concentration (PO₄),

$$\text{NPP} = \alpha \frac{\text{PAR}}{\text{PAR} + K_{\text{PAR}}} \frac{\text{PO}_4}{\text{PO}_4 + K_{\text{PO}_4}} \quad (1)$$

where $\alpha = 2 \times 10^{-3} \text{ mol m}^{-3} \text{ yr}^{-1}$ is the maximum community productivity, $K_{\text{PAR}} = 30 \text{ W m}^{-2}$ the half saturation light constant, and $K_{\text{PO}_4} = 5 \times 10^{-4} \text{ mol m}^{-3}$ the half saturation phosphate constant. Two thirds of the biological production remains suspended in the water column as dissolved organic phosphorus (DOP), which remineralizes back to phosphate following an e-folding time scale of 6 months [Yamanaka and Tajika, 1997]. The remainder of the biological production sinks to depth as particulate organic phosphorus (POP) and remineralizes according to the empirical power law of Martin *et al.* [1987]. The oceanic residence time of phosphate is estimated between 10 and 40 kyrs [Ruttenberg, 1993; Wallmann, 2003], much longer than the oceanic turnover time scale. The globally averaged oceanic phosphate concentration is therefore fixed in the model. Riverine and atmospheric sources are not represented and sedimentation is not allowed [Dutkiewicz *et al.*, 2005]. Phosphate is consumed to fuel the marine primary productivity in the photic zone, regenerated by remineralization in the water column and ultimately advected-diffused by the global ocean circulation back to the ocean surface in upwelling zones. In the present setup, phosphate constitutes the single limiting nutrient. Iron is known to significantly constrain primary productivity as well [e.g., Falkowski, 2012]. It is essentially supplied to the ocean through atmospheric deposition of mineral dust originating from deserts. Present-day iron dust emissions and flux, however, remain difficult to quantify [e.g., Bryant, 2013]. Reconstructing their Early Paleozoic counterparts is challenging, notably implying major assumptions on the land surface typology. Although our biogeochemistry model does have the provision for explicitly representing cycling of iron, we therefore choose not to consider iron fertilization in the present study. Oxygen is exchanged at the ocean-atmosphere interface following Garcia and Gordon [1992] and redistributed within the ocean using the velocity and diffusivity fields provided by the general circulation model. The fate of O₂, i.e., transformation to and from organic form, is also tied to that of phosphorus through fixed Redfield stoichiometry. The PAR is defined at the surface of the ocean as the fraction of the incident shortwave radiation that is photosynthetically available. It is then attenuated as it travels through the water column assuming a uniform extinction coefficient. The shortwave radiation is provided by the atmospheric component of our coupled climate model. Similar configurations of the biogeochemistry model were used in the past [e.g., Friis *et al.*, 2006, 2007].

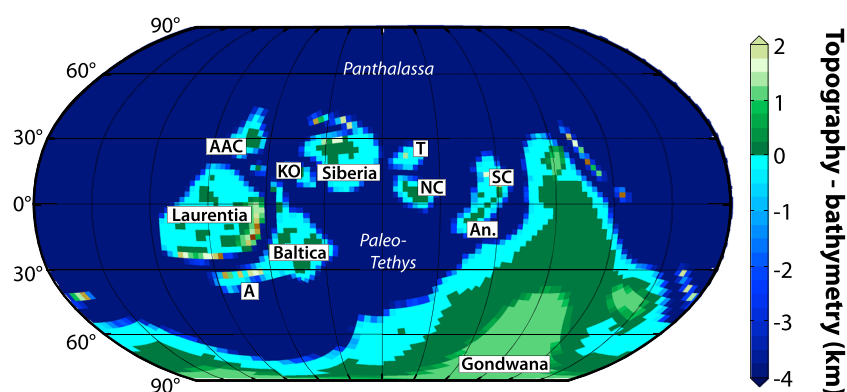


Figure 1. Late Ordovician-early Silurian continental reconstruction interpolated on the MITgcm cubed sphere grid: AAC: Arctic Alaska-Chukotka, KO: Kolyma-Omolon, A: Avalonia, T: Tarim, NC: North China, SC: South China, An: Annamia. Ocean names are in italic.

2.2. Boundary and Initial Conditions

Because the geological events under study occurred over a duration that is lower than the temporal resolution of current paleogeographical reconstructions, we use a single continental configuration to simulate climate throughout the whole Ordovician-Silurian boundary. We use the Late Ordovician paleogeography from *Torsvik and Cocks* [2009]. The topography and bathymetry are reconstructed based on studies for Gondwana [Torsvik and Cocks, 2013], Laurentia [Cocks and Torsvik, 2011], Baltica [Cocks and Torsvik, 2005], Siberia [Cocks and Torsvik, 2007], and for modern Asia [Cocks and Torsvik, 2013]. Because the location of ocean ridges is highly speculative in the Ordovician, they are not included in our reconstruction (i.e., we prescribe a flat bottom). The resulting map (Figure 1), given in input to the model, is identical to the one used by *Pohl et al.* [2016a, see their Figure 2a]. Because vegetation was restricted to nonvascular plants during the Ordovician [Steenmans et al., 2009; Rubinstein et al., 2010], the spatial cover of which is difficult to estimate and largely debated [e.g., Porada et al., 2016; Heckman et al., 2001; Edwards et al., 2015], we follow previous studies [Nardin et al., 2011; Pohl et al., 2014, 2016a, 2016b] and impose a rocky desert on continents (prescribed ground albedo of 0.24, which is modified by snow if present). The orbital configuration is defined with an eccentricity of 0° and an obliquity of 23.45°. The same initial conditions are used in all simulations. The temperature distribution is defined by a theoretical latitudinal temperature gradient, characterized by equatorial and polar ocean surface temperatures of respectively 35°C and 6°C, and an ocean bottom initial potential temperature of 3°C. Ocean is therefore sea ice free at the beginning of each simulation. A uniform initial salinity of 35 psu (practical salinity units) is imposed over the whole domain. Phosphate and oxygen in the ocean are initialized with present-day depth profiles, and DOP is null at the beginning of the simulation. Reconstructions of the Ordovician atmospheric partial pressure of oxygen (pO_2) lead to scattered values. *Bergman et al.* [2004] and *Berner* [2006, 2009], using models of biogeochemical cycling, propose values between respectively 0.2 to 0.6 and 0.72 to 0.95 times the present-day level. *Algeo and Ingall* [2007] estimate, by inversion of the Phanerozoic C_{org} :P curve, that the Ordovician pO_2 was between 0.61 and 0.8 times the current level. Given the large uncertainty in these reconstructions, the atmospheric oxygen partial pressure is kept to its present-day level in the model, and sensitivity tests are conducted for pO_2 values ranging between 0.2 and 0.8 times the current value in order to cover the large uncertainties in estimates for the Ordovician. It is noteworthy that in those tests, the changes in pO_2 only affect the ocean-atmosphere gas exchange. They do not alter the radiative fluxes as proposed in the recent study by *Poulsen et al.* [2015]. Our coupled ocean-atmosphere-sea ice-land surface model (see section 2.1.1) is first run until deep-ocean equilibrium is reached (≥ 2000 years). It is subsequently restarted with the biogeochemistry module (section 2.1.2) for at least 550 additional years (1550 for the sensitivity tests using a reduced pO_2 , since the initial (present-day) oxygen concentration significantly differs from the equilibrium state in these runs), the last 50 years of which are used to build the climatology files used for analysis (Figure S1 in the supporting information).

3. Climatic Simulations

Here we simulate various climate states (section 3.1) and subsequently select the model outputs that best reflect the climatic conditions prevailing during each of the three time slices used in the black shale

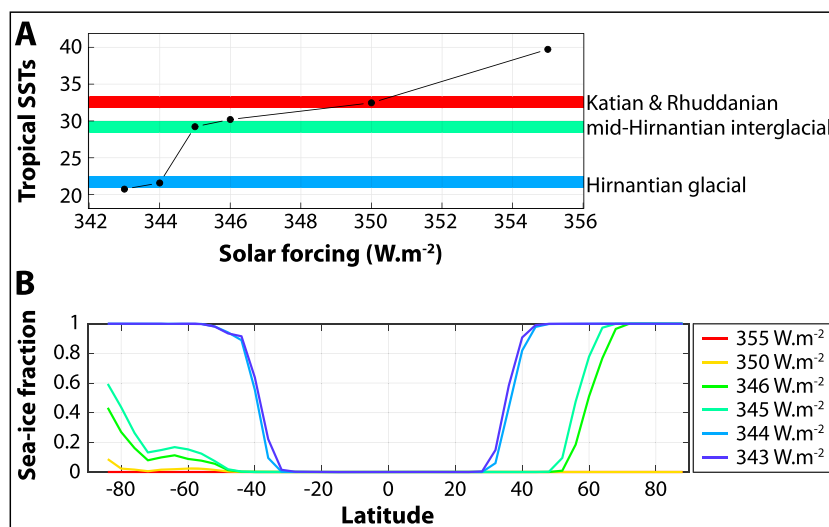


Figure 2. Climate results. (a) Mean annual tropical (30°S – 30°N) sea surface temperatures as a function of the solar forcing level. We here represent the tropical sea surface temperatures (SSTs), instead of the global surface air temperatures, because Ordovician and Silurian isotopic data are gathered in locations situated at low paleolatitudes. As a consequence they exclusively report variations in tropical SSTs, which thus constitute the most straightforward variable for any model-data comparison [e.g., Trotter *et al.*, 2008; Finnegan *et al.*, 2011]. The colored strips identify the simulations selected throughout this study to investigate the mechanisms governing the deposition of black shales in the three time slices documented by Melchin *et al.* [2013]: the late Katian (red), the mid-Hirnantian (green), and the early Rhuddanian (red as well). The Hirnantian glacial state is shown for comparison (blue), but the associated model run is not analyzed in detail in this study. Please note that the colors of the strips correspond to the colors of the lines drawn in Figure 2b. (b) Mean annual latitudinal sea ice fraction simulated at various solar forcing levels.

compilation of Melchin *et al.* [2013]: the late Katian, the mid-Hirnantian, and the early Silurian Rhuddanian (section 3.2).

3.1. Model Results

The atmospheric component of our model, SPEEDY, does not account for varying $p\text{CO}_2$ levels. The radiative code is parametrized to reproduce present-day-like greenhouse gas concentration (see section 2.1.1). The simulation of different climatic conditions is thus achieved by varying the solar forcing in the model [e.g., Ferreira *et al.*, 2011]. Results are displayed in Figure 2. Simulated tropical sea surface temperatures (SSTs) linearly decrease with the external forcing level, except between 345 W m^{-2} and 344 W m^{-2} . At this point, a decrease of 1 W m^{-2} induces a large drop in tropical SST of 7.6°C (Figure 2a).

Pohl *et al.* [2014] studied the response of the Ordovician climate system to a decrease in $p\text{CO}_2$. They demonstrated, using the Fast Ocean Atmosphere Model (FOAM) [Jacob, 1997] and Blakey's [2016] Late Ordovician continental reconstruction, that there is a radiative forcing level (~ 2240 ppm CO_2) beyond which Ordovician climate suddenly shifts from a warm state with limited sea ice extent in the Northern Hemisphere, to a much colder state characterized by the sudden extension of the sea ice to the middle-to-tropical latitudes. Building on previous work investigating the presence of multiple equilibria in aquaplanets [Rose and Marshall, 2009; Ferreira *et al.*, 2011], they demonstrated that this climatic instability results from the absence of meridional continental boundaries in the Ordovician Northern Hemisphere. These conditions limit the ocean heat transport to the pole and facilitate the growth of large sea ice caps. In our study, a similar climatic behavior is obtained. The large cooling simulated between 345 W m^{-2} and 344 W m^{-2} is due to the ice-albedo positive feedback associated with the spread of sea ice (Figure 2b [see Pohl *et al.*, 2014]).

3.2. Simulating Katian, Mid-Hirnantian, and Early Silurian Climate

Over the last decade, prominent insights into the Ordovician-Silurian climatic fluctuations were independently provided by Trotter *et al.* [2008, 2016] and Finnegan *et al.* [2011]. Based respectively on tropical $\delta^{18}\text{O}_{\text{apatite}}$ and $\Delta^{47}\text{CO}_2$ data, they reconstructed temperature trends similar to the $\delta^{18}\text{O}_{\text{brach}}$ - and $\delta^{18}\text{O}_{\text{bulk}}$ -derived SSTs published a decade prior [Long, 1993; Brenchley *et al.*, 1994, 1995, 2003], except that the SST values calculated from these new proxy data fall within an acceptable modern-like SST range, significantly contrasting with the unlikely previous ocean temperature estimates of up to $\sim 70^{\circ}\text{C}$. Trotter *et al.* [2008] and Finnegan *et al.* [2011]

notably demonstrated a sudden, sharp drop in tropical SSTs by $\sim 7^{\circ}\text{C}$ during the latest Ordovician Hirnantian (445–444 Ma). They also suggested that Ordovician climate was relatively warm before the Hirnantian, with Katian (~ 450 Ma) tropical SSTs ranging between $\sim 30^{\circ}\text{C}$ [Trotter *et al.*, 2008] and 35°C [Finnegan *et al.*, 2011]. Among the various climate states simulated in this study (see Figure 2), the simulation with a solar forcing of 350 W m^{-2} is characterized by a mean tropical SST of 32.5°C . In the following, we consider this simulation as representative of the Katian climate state documented by most recent studies [Trotter *et al.*, 2008; Finnegan *et al.*, 2011, Figure 2a].

Following the relatively warm late Katian period, the latest Ordovician Hirnantian (445–444 Ma) glacial peak is typified by a sudden global climate cooling [Trotter *et al.*, 2008; Finnegan *et al.*, 2011] and the growth of a continental-scale ice sheet over the South Pole [Denis *et al.*, 2007; Ghienne *et al.*, 2007; Le Heron and Craig, 2008; Loi *et al.*, 2010]. During the mid-Hirnantian (upper *extraordinarius*–lower *persculptus* Zone, in the sense of Melchin *et al.* [2013]), the land ice front temporarily retreats over Gondwana [Sutcliffe *et al.*, 2000; Loi *et al.*, 2010; Moreau, 2011] and tropical SSTs increase back [Finnegan *et al.*, 2011; Melchin *et al.*, 2013], which lead some authors to consider this event as an interglacial [Denis *et al.*, 2007; Ghienne *et al.*, 2007; Loi *et al.*, 2010; Young *et al.*, 2010; Moreau, 2011; Melchin *et al.*, 2013]. Pohl *et al.* [2014] proposed that the nonlinear Ordovician temperature response, simulated in this study when decreasing solar luminosity from 345 W m^{-2} to 344 W m^{-2} , may provide an explanation to the otherwise enigmatic sudden Hirnantian climate cooling. This hypothesis suggests that the simulation conducted at 344 W m^{-2} may be the most representative of the Hirnantian climate. Although this very cold state may adequately represent the periods of Hirnantian glacial advance, we here focus on the mid-Hirnantian interglacial when climate was significantly warmer as testified by the retreat of the ice front in North Africa and in the Middle East [e.g., Ghienne *et al.*, 2007; Moreau, 2011]. We therefore consider that the simulation at 345 W m^{-2} best reflects the climatic conditions prevailing during the mid-Hirnantian interglacial (Figure 2a). The annual-mean, globally averaged surface air temperature in this model run is 17.1°C , compared to 23.4°C at 350 W m^{-2} . From a radiative point of view, a halving of the atmospheric CO_2 concentration corresponds to a radiative perturbation of -3.7 W m^{-2} at the top of the atmosphere [Myhre *et al.*, 1998]. The decrease in solar luminosity accounting for the Hirnantian climate cooling in our simulations (from 350 W m^{-2} to 345 W m^{-2}) is therefore equivalent to a decrease of $p\text{CO}_2$ by a factor 2.7, or equally to a decline of $p\text{CO}_2$ from 8 times the preindustrial atmospheric level (8 PAL, 1 PAL = 280 ppm) during the late Katian to 3 PAL (or 12 PAL to 4.5 PAL). The magnitude of this decrease in radiative forcing is in reasonable agreement with the estimates recently proposed by Pohl *et al.* [2016b]. Using an innovative coupling method between climate models and an ice sheet model, they conducted the first simulation of Ordovician land ice growth that is supported by the geological record. In their models, best match with data is obtained between 8 PAL and 12 PAL during the late Katian, and at 3 PAL during the Hirnantian (see their Figure 9). We emphasize that we do not investigate the climatic impact of the growth of the Hirnantian ice sheet over the South Pole in the present study but identify this as a target for the future.

The latest Hirnantian–early Rhuddanian period is characterized by the continental-scale decay of the Gondwana ice sheet [Finnegan *et al.*, 2011; Moreau, 2011; Denis *et al.*, 2007; Loi *et al.*, 2010; Le Heron *et al.*, 2009]. Trotter *et al.*'s [2008] data do not extend into the Silurian, thus hampering any appraisal of the climatic conditions relative to mid-Ordovician levels. The clumped-isotope analysis of Finnegan *et al.* [2011], however, suggests that tropical SSTs rapidly rise in the aftermath of the Hirnantian glacial peak and reach pre-Hirnantian levels as early as the latest Hirnantian ($\sim 35^{\circ}\text{C}$). This value is supported by the Telychian (~ 435 Ma) estimate of $34.9 \pm 0.4^{\circ}\text{C}$ reported by Came *et al.* [2007] in a previous study on Anticosti Island. We therefore assume that the solar forcing level chosen previously to study the Katian (350 W m^{-2}) satisfactorily represents the Rhuddanian time slice as well (Figure 2a).

4. The Late Katian

In the compilation of Melchin *et al.* [2013], black shale deposition in the late Katian occurred mainly at tropical to subtropical paleolatitudes on the western margin of the equatorial landmasses. On the contrary, the northern margin of Gondwana and the platforms surrounding Baltica were typified by oxic deposits (see Figure 3a). Here we examine the simulation conducted at 350 W m^{-2} in order to disentangle the respective contributions of surface primary productivity and dissolved oxygen concentration in the formation of the pre-Hirnantian black shales.

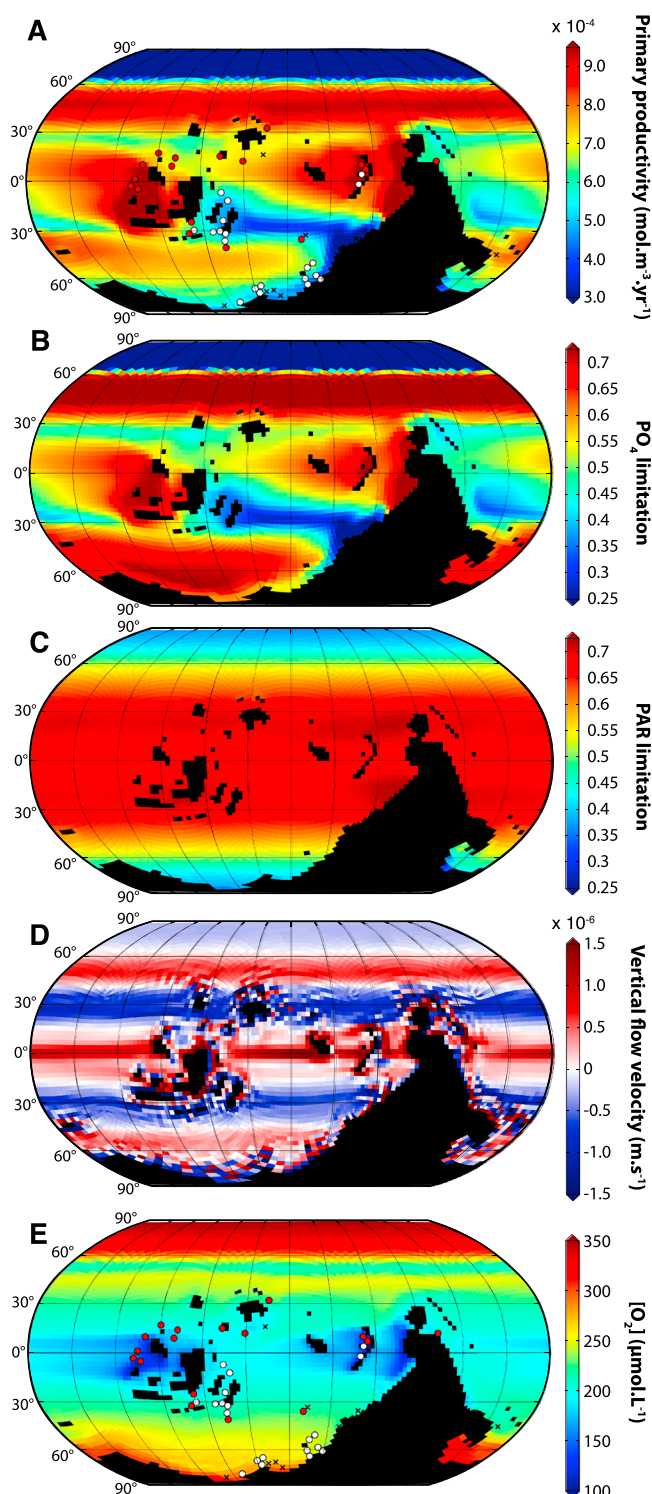


Figure 3. Analysis of the patterns of marine primary productivity and oxygen concentration simulated using the 440 Ma land-sea mask and a solar forcing level of 350 W m^{-2} . (a) Surface primary productivity. White and red dots respectively stand for sediments of Katian age associated with dysoxic-to-oxic and at least intermittently anoxic conditions (i.e., black shales, including interbedded black shales), after the compilation of Melchin *et al.* [2013]. (b) Contribution of surface phosphate concentration to the primary productivity (third term in equation (1)). (c) Contribution of the PAR to the surface primary productivity (second term in equation (1)). (d) Vertical velocity averaged over the first 50 m of the water column. Positive values correspond to upwelling water masses. (e) Oxygen concentration simulated at the depth of the epicontinental seas in the model (80 m), with Katian data points from Melchin *et al.* [2013]. See Figure S2 for identification of the data points following the original numbering from Melchin *et al.* [2013].

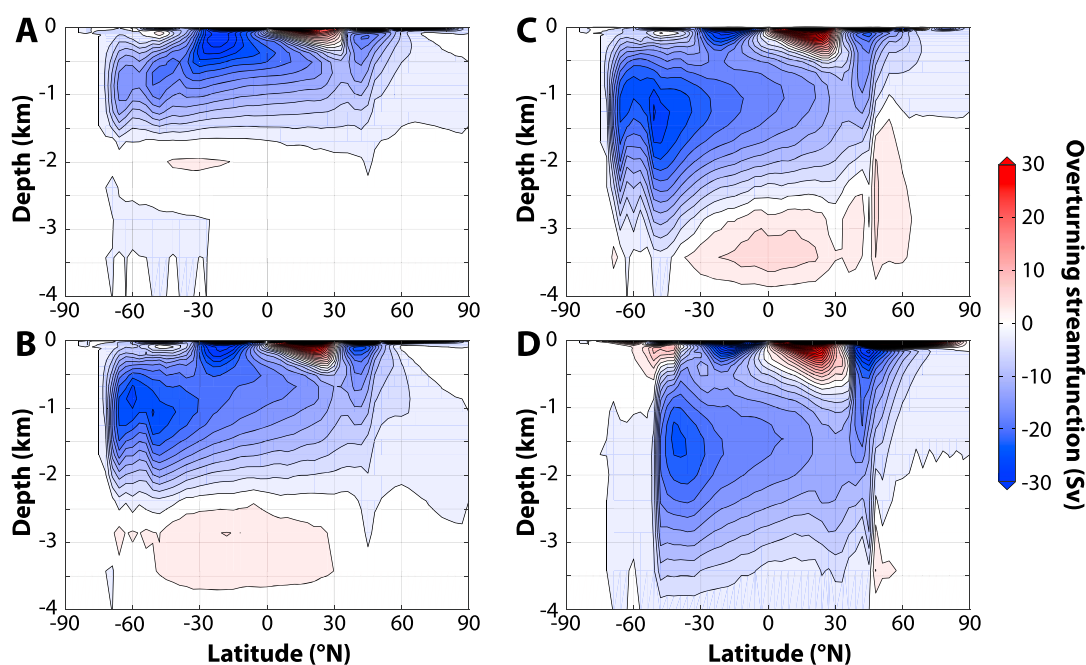


Figure 4. Meridional overturning stream function simulated using solar constant values of (a) 355 W m^{-2} , (b) 350 W m^{-2} , (c) 345 W m^{-2} , and (d) 344 W m^{-2} . The stream function is computed as the sum of the Eulerian and eddy-induced circulations. The contour interval is 2.5 Sv (sverdrup, $1 \text{ Sv} = 10^6 \text{ m}^3 \text{ s}^{-1}$). A negative (blue) stream function corresponds to an anticlockwise circulation. Results from the two end-member model runs conducted at 355 W m^{-2} and 344 W m^{-2} are shown here to highlight the deepening trend in the meridional overturning stream function. They are not discussed in the main text. Main patterns of the simulated overturning stream function are in agreement with previous studies of *Poussart et al.* [1999] and *Herrmann et al.* [2004].

4.1. Simulating the Late Katian Marine Primary Productivity

Figure 3a displays the NPP simulated using a solar forcing level of 350 W m^{-2} , together with the individual contributions of phosphate concentration (Figure 3b, third term in equation (1)) and photosynthetically active radiation (Figure 3c, second term in equation (1)) in the simulated NPP. While the limitation in PO_4 (Figure 3b) is the main driver of the primary productivity pattern (Figure 3a), the availability of light imposes a hemispheric-scale decrease of the productivity with latitude (Figure 3c).

The distribution of PO_4 (Figure 3b) in the surface waters is controlled by the large-scale pattern of vertical velocities just below the surface of the ocean, which are dominated by Ekman pumping/suction (Ekman transport [Ekman, 1905]).

1. Along the equator, the trade winds induce the divergence of the ocean water masses, resulting in equatorial upwelling (Figure 3d; see also Figure 4). These equatorial winds further drive offshore Ekman transport along the western margin of the tropical continental masses, i.e., Laurentia, South China-Annamia, and the Gondwana, allowing cold, nutrient-rich water to upwell from the deep ocean (Figure 3d; see Figure 1 for the name and location of each continent). An intense surface primary productivity is therefore simulated at these latitudes (Figure 3a).
2. Low levels of phosphate concentration are simulated around 30°S and 30°N (Figure 3b). Between the trades, at tropical latitudes, and the Westerlies, at the midlatitudes, the ocean realm centered on 30°N/S is typified by the convergence and sinking of low-phosphate surface waters (Figure 3d). This corresponds to the poleward edge of the tropical cells of the oceanic overturning circulation (Figure 4d). In the Paleo-Tethys, between eastern Baltica and the western coast of Gondwana (Figure 5a), the downwelling of surface waters further combines with a strong freshwater flux from the continent (Figures 5b and 5c), forming a zone of minimum phosphate concentration (Figure 5a) and thus minimum primary productivity (Figure 3a). In detail, moisture-laden air masses originating from the Paleo-Tethys are conveyed by the Westerlies to the western coast of Gondwana. Further inland, intense orographic precipitation occurs and the amount of liquid water exceeding the field capacity of the soil is delivered to the ocean (Figure 5c), where the freshwater flux induces a strong dilution of both salinity (Figure 5b) and phosphate (Figure 5a). It is noteworthy that, using the same paleogeography but another ocean-atmosphere general circulation model

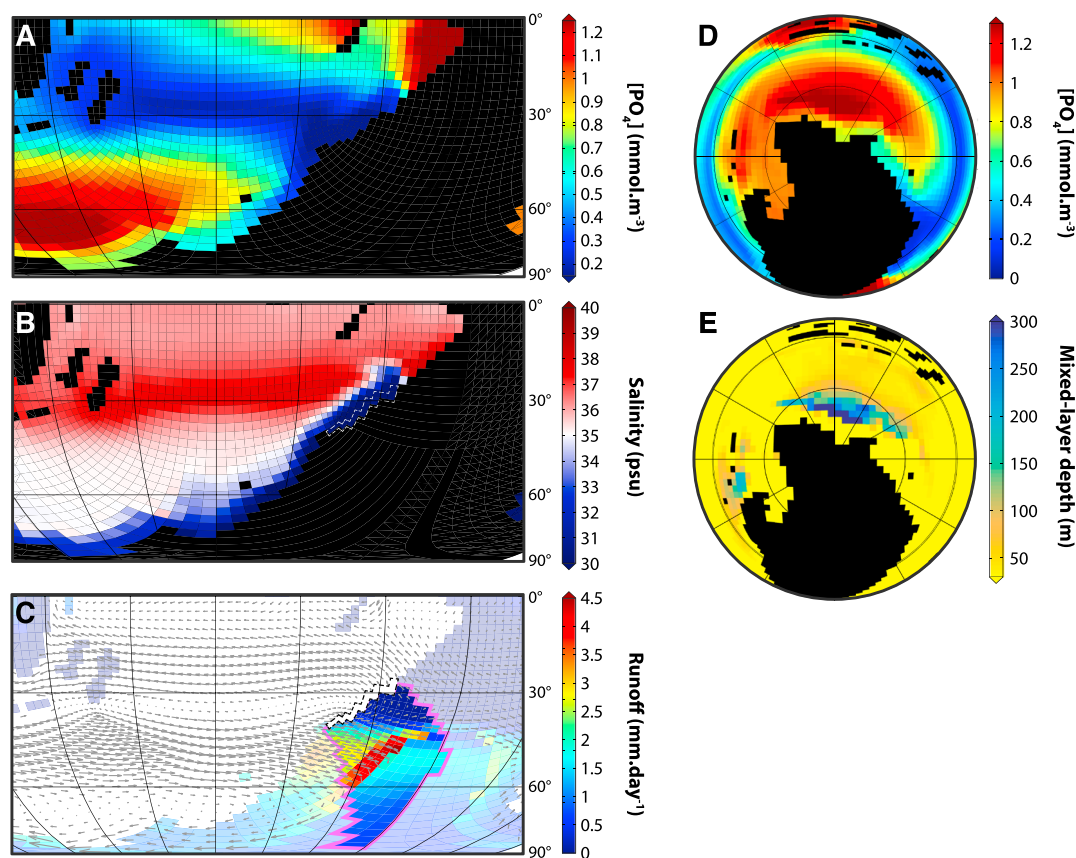


Figure 5. Analysis of the patterns of mean annual, surface phosphate concentration simulated using the 440 Ma continental land-sea mask and a solar forcing level of 350 W m^{-2} . (a) PO_4 concentration in the Paleo-Tethys. (b) Ocean surface salinity in the Paleo-Tethys. (c) Near-surface winds (vectors) and continental runoff (shading) simulated in the same region. The pink contour delimits the watershed associated with the outlet constituted by the points highlighted with the dashed white line in Figure 5b, which correspond in turn to a zone of minimum of salinity. Grid points with no vectors are mountainous areas. Runoff here refers to the amount of water that is transferred from the continental grid points to the ocean (no routine scheme is implemented in this configuration of the model, see section 2.1.1). (d) South polar projection map of surface phosphate concentration. Laurentia is shown on top of the map. (e) South polar projection map of mixed-layer depth.

employing an explicit routing scheme for runoff and a more sophisticated atmospheric component (FOAM) [Jacob, 1997], Pohl et al. [2016a] simulated very similar regional patterns of runoff and freshwater input to the ocean (Figure S3). In addition, most Ordovician paleogeographical reconstructions seem to concur regarding the presence of highlands over Gondwana at these latitudes, which are likely to promote intense precipitation and runoff along the western coast of the supercontinent [Blakey, 2016; Scotese, 2016].

- Between 40° and 60° , the Westerlies drive an equatorward Ekman transport and deep-water upwelling (Figure 3d). The dynamical regime of the Northern high-latitude Ordovician is similar to that seen in the present-day Southern Ocean with its Antarctic Circumpolar Current [Marshall and Speer, 2012] (see Figure 4). As a consequence, phosphate-rich waters are brought up to the ocean surface (Figure 3b) where they fuel the surface primary productivity (Figure 3a).
- Whereas the Northern Hemisphere polar latitudes ($60^\circ - 90^\circ$) are dynamically isolated from the global ocean (Figure 4b) and thus depleted in nutrients (Figure 3b), the southern high-latitudes are typified by a strong nutrient supply (Figure 3b). The latter spatially correlates with a deep mixed layer (Figures 5d and 5e) and results from the intense deep convection and intense vertical exchange with nutrient-rich deep waters along the northern margin of Gondwana (Figure 4b). The location of this zone of intense convection is supported by previous studies [e.g., Herrmann et al., 2004] (see also Figure S4). In the Southern Hemisphere, combined imprints of the Westerlies (at the midlatitudes) and of deep-water convection (at polar latitudes) result in a large zone of nutrient-rich waters extending from $\sim 40^\circ\text{S}$ to the South Pole (Figure 3b). Over the

Pole along the coast of Gondwana, however, the high levels of phosphate concentration do not directly translate into intense primary productivity (Figure 3a) because of the limited incoming solar radiation (Figure 3c).

4.2. Black Shale Deposits and the Redox State of the Ocean

Comparison of the patterns of simulated primary productivity with the database of *Melchin et al.* [2013] (Figure 3a) reveals an interesting match between high-productivity areas (low-productivity areas) and geologically testified preservation of black shales (oxic deposits). This correlation is summarized with boxplots in Figure 6a.

We seek to determine whether the difference between the primary productivity simulated at localities typified by the deposition of black shales on the one hand and typified by oxic conditions on the other hand [after *Melchin et al.*, 2013] (see Figure 3a and Figure 6a) is significant from a statistical point of view. We choose the Wilcoxon-Mann-Whitney test [R Core Team, 2013]. This is a basic nonparametric test of the null hypothesis that the two samples come from the same population (H_0 : levels of primary productivity simulated where black shales are preserved do not significantly differ from the values simulated where oxic deposits are documented). The alternative hypothesis is that a particular population tends to have larger values than the other (H_1 : primary productivity in the model is significantly higher where black shales are preserved than they are at oxic localities). Unlike the t test, the Wilcoxon-Mann-Whitney test does not require the assumption of normal distributions, which is crucial in our study given the limited number of Ordovician observations in *Melchin et al.*'s [2013] database. The result of the test is expressed as a p -value. If the p -value is less than the significance level chosen (e.g., p value < 0.05), then the test suggests that the observed data is inconsistent with the null hypothesis, so the null hypothesis H_0 must be rejected and the alternative hypothesis H_1 accepted: the two samples do not come from the same population.

The Wilcoxon-Mann-Whitney test confirms that the two samples—the black shales and oxic deposits, red and white data points in Figure 3a—represent two populations characterized by significantly distinct levels of primary productivity (p value: $6.53 \times 10^{-5} < 0.05$, H_0 is rejected). Three different sets of points can be distinguished within the oxic data points reported by *Melchin et al.* [2013]. The first group is composed of the two outliers deduced from Figure 6a. They correspond to the two points located in the high-productivity area along the western coast of South China and Annamia (Figure 3a). Other data points can be gathered into two groups depending on whether they belong to the cluster of points situated around Baltica or along the northern margin of Gondwana (Figure 3a). Interestingly, both clusters seem to be relatively similar to each other (Figure 6a), and a Wilcoxon-Mann-Whitney test confirms that they come from the same statistical population (p value: $0.762 > 0.05$, H_0 is accepted). It appears that the correlation between low marine productivity and oxic deposition is relatively strong, except for the two outliers highlighted previously.

At the depth of the epicontinental shelves, the oxygen concentration increases from the equator to the poles (Figure 3e). This gradient reflects the higher solubility of oxygen in cold waters. Superimposed on this purely thermal effect is the imprint of ocean dynamics. The western margin of the equatorial continental masses, in particular, is washed by oxygen-poor waters upwelling from deeper parts of the ocean. Because they are rich in nutrients, these waters promote regional primary productivity (Figure 3a), which in turn increases remineralization in the water column and thus enhances oxygen depletion at depth. Geological evidence for organic matter preservation spatially correlates with oxygen levels that are, in the model, significantly lower than those simulated at oxic localities (Figures 3e and 6b, p value: $0.0016 < 0.05$ for the two-sided Wilcoxon-Mann-Whitney test). However, the points associated with conditions of oxic sedimentation actually include two significantly contrasting populations (p value: $4.571 \times 10^{-5} < 0.05$): the points clustering along the coast of Gondwana are typified by high oxygen levels, whereas the points around Baltica do not significantly differ from the “black shale” population (Figure 6b, p value: $0.075 > 0.05$).

4.3. Sensitivity to the pO_2

The regions where black shales are preserved in the Katian sedimentary record [*Melchin et al.*, 2013] correlate well with the areas of high surface primary productivity simulated under a warm climate representative of pre-Hirnantian conditions. Conversely, the preservation of sediments testifying of oxic depositional settings is documented in regions where the simulated primary productivity is low. The spatial correlation between geological proxies of ocean redox state and simulated oxygen concentration is less obvious. These results

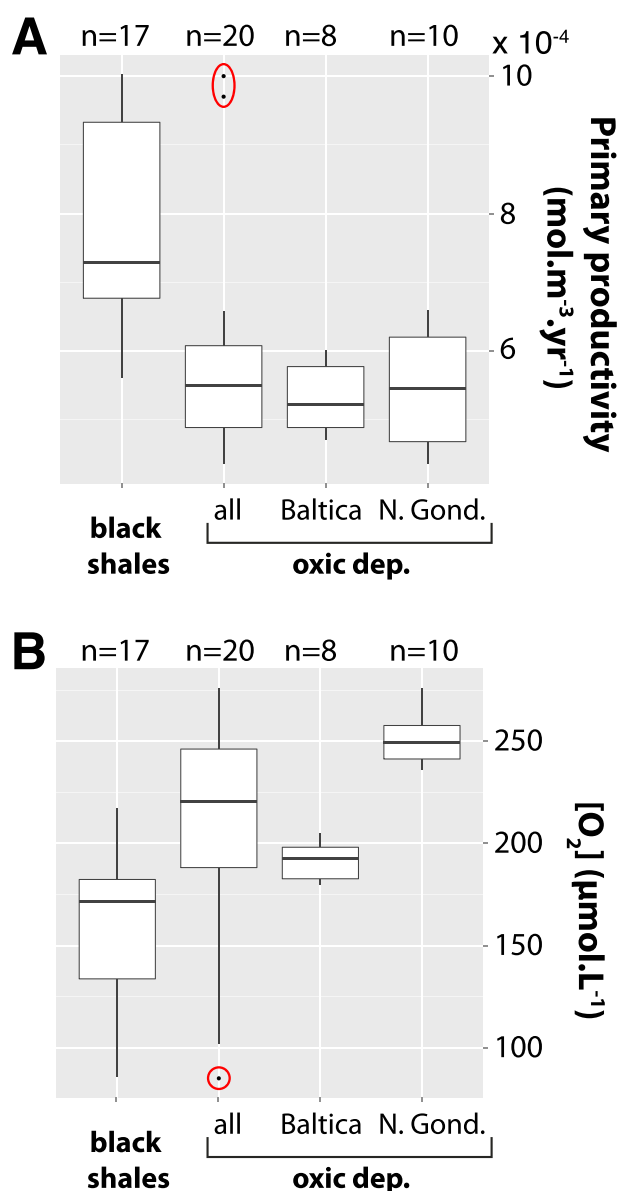


Figure 6. Boxplots of (a) primary productivity at the ocean surface and (b) oxygen concentration at the depth of the epicontinental seas (80 m), simulated using the 440 Ma land-sea mask and a solar forcing level of 350 W m^{-2} at each Katian data point from Melchin et al. [2013]. For statistical analysis, points are gathered into samples depending on whether sediments were deposited under oxic ("oxic dep., all") or anoxic conditions ("black shales"), after Melchin et al. [2013] (white and red dots in Figure 3a, respectively). Oxic sediments situated around Baltica (see "Baltica" in the legend) and along the margin of Gondwana ("N. Gond.") are further extracted for dedicated investigation. The group gathering all the $n = 20$ "oxic deposits" points therefore includes the $n = 8$ data points around Baltica, plus the $n = 10$ data points situated along the northern margin of Gondwana and the two points between South China and Annamia (i.e., the two outliers in Figure 6a; see Figure 3a). The box represents the interquartile range (or IQR, i.e., distance between the first and the third quartiles), and the band inside the box is the second quartile (i.e., the median). The upper and lower whiskers respectively extend from the box to the highest (lowest) value that is within $1.5 \times \text{IQR}$ beyond the box edges, and data beyond the end of the whiskers (circled in red) are outliers, following Tukey [1977].

suggest that the spatial distribution of the black shales deposited during the Katian may have been mainly driven, at a global scale, by surface primary productivity levels rather than variations in dissolved oxygen concentration.

Nevertheless, when it is run on the present-day continental configuration, our model simulates, over extended areas that are devoid of black shales today, levels of surface primary productivity that reach the values

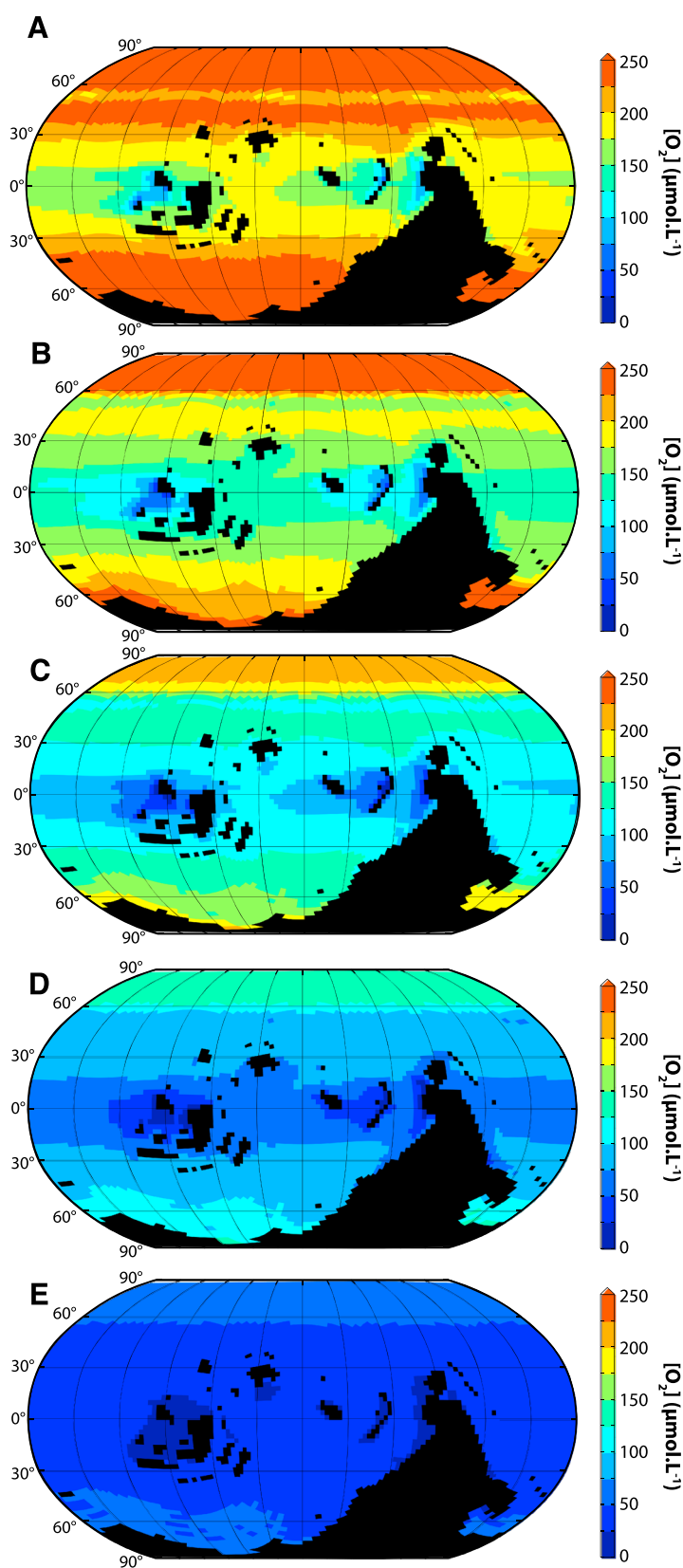


Figure 7. Sensitivity test to the pO_2 -oxygen concentration simulated at the depth of the epicontinental seas in the model (80 m), using the 440 Ma land-sea mask, a solar forcing level of 350 W m^{-2} and an atmospheric pO_2 set to (a) 1.0, (b) 0.8, (c) 0.6, (d) 0.4, and (e) 0.2 times the present-day value.

associated with the deposition of black shales during the Katian (Figure S5). This points to major differences between the Ordovician and present-day oceans, which would have augmented the potential for organic matter burial in the Early Paleozoic.

Biogeochemical models and inversion methods notably indicate that the pO_2 was significantly lower in the Ordovician, probably between 0.2 and 0.8 times the present-day levels [Bergman *et al.*, 2004; Berner, 2006; Algeo and Ingall, 2007; Berner, 2009; Lenton *et al.*, 2016]. Sensitivity tests confirm that atmospheric oxygen levels in this range significantly reduce the oxygenation of the ocean at the depth of the epicontinental seas in the model (Figure 7; see also Figure S6 for depth profiles over the whole water column). Between 0.4 and 0.2 PAL O_2 , the tropics exhibit low concentrations of dissolved oxygen ($<75 \mu\text{mol L}^{-1}$) that would significantly reduce the rate of degradation of the settled organic matter (Figures 7d and 7e). The absence of charcoal in the Ordovician sedimentary record further suggests that the pO_2 was sufficiently low as to prevent the sustained combustion of plant material ($<13\%$) [Chaloner, 1989; Algeo and Ingall, 2007], supporting the lowest estimates from the pO_2 range above. With a pO_2 set to 0.2 times the present-day level, the ocean oxygen content drops below $50 \mu\text{mol L}^{-1}$ over virtually the entire ocean realm, except in the Northern Hemisphere highest latitudes and at the location of deep-water formation in the Southern Hemisphere (Figure 7e).

We argue that the lowered Early Paleozoic pO_2 (≤ 0.4 PAL O_2 , Figure 7), combined with exceptionally vast shallow-water environments [Walker *et al.*, 2002] resulting from the highest sea level during the whole Paleozoic Era [Haq and Schutter, 2008], largely predisposed the Ordovician ocean to organic matter preservation. Our results suggest that in this particular context, the deposition of black shales in tropical settings may have been driven by the patterns of surface primary productivity. Our simulations also imply that the two data points characterized by unexpected oxic depositional settings in South China—the two outliers highlighted in Figure 6a, points No. 25 and No. 26 from Melchin *et al.* [2013]—may reflect local redox conditions typifying basins that were at least partially disconnected from the open ocean.

5. The Hirnantian Glacial Pulse

The latest Ordovician Hirnantian is characterized by a sudden drop in tropical SSTs [Trotter *et al.*, 2008; Finnegan *et al.*, 2011]. It represents the climax of the Ordovician glaciation [Page *et al.*, 2007; Finnegan *et al.*, 2011; Pohl *et al.*, 2016b]. The compilation of Melchin *et al.* [2013] reports a worldwide change to more oxygenated depositional settings at this time. In order to investigate the mechanisms driving this possible mid-Hirnantian oceanic oxygenation event, we here study the response of Ordovician marine biogeochemistry to climate cooling.

5.1. Response of the Ocean Redox State to Climate Cooling

For these experiments, we lower the incoming solar radiation in order to simulate a climate cooling (from 350 W m^{-2} to 345 W m^{-2} , see section 3). As a consequence, tropical SSTs drop from 32.5 to 29.2°C (Figure 2a). This also artificially induces a slight (-1.5%) decrease in simulated net primary productivity, through a drop in photosynthetically available radiation, following equation (1).

Climate cooling does not critically impact the first-order patterns of simulated primary productivity (Figure 8a). The prominent change accompanying the drop in temperature is the increase in oxygen concentration throughout the water column (Figure 8b). The latter results from two main mechanisms. First, oxygen solubility in ocean water increases with decreasing temperature. A straightforward effect of this is a more intense air-sea exchange of oxygen at the ocean surface in the coldest simulation. This directly affects the first tens of meters of the water column, the so-called mixed layer, and then the deeper layers as currents and mixing processes carry the enhanced surface oxygenation in the ocean interior (Figure 8b). Second, the meridional overturning circulation intensifies and deepens (compare Figures 4b and 4c) in response to climate cooling and associated sea ice spread (Figure 2b), thus enhancing the ventilation and the oxygenation of the deep ocean. Interestingly, the oxygenation of the deep ocean is not uniform in space. As shown in Figures 8c and 8d, the increase in ocean bottom oxygen concentration reaches its maximum where Ordovician deep waters form (see Figure 5e). On the contrary, the water masses that sink along the northern margin of Gondwana do not enter the Paleo-Tethys realm, which is virtually isolated from the global ocean. This area is characterized by low oxygen levels in the 350 W m^{-2} model run, with a global minimum located over South China-Annamia (Figure 8c). When solar forcing is decreased, the whole Paleo-Tethys displays a very limited pO_2 increase (Figure 8d). Results of additional simulations using a pO_2 reduced to 0.4 times the present-day

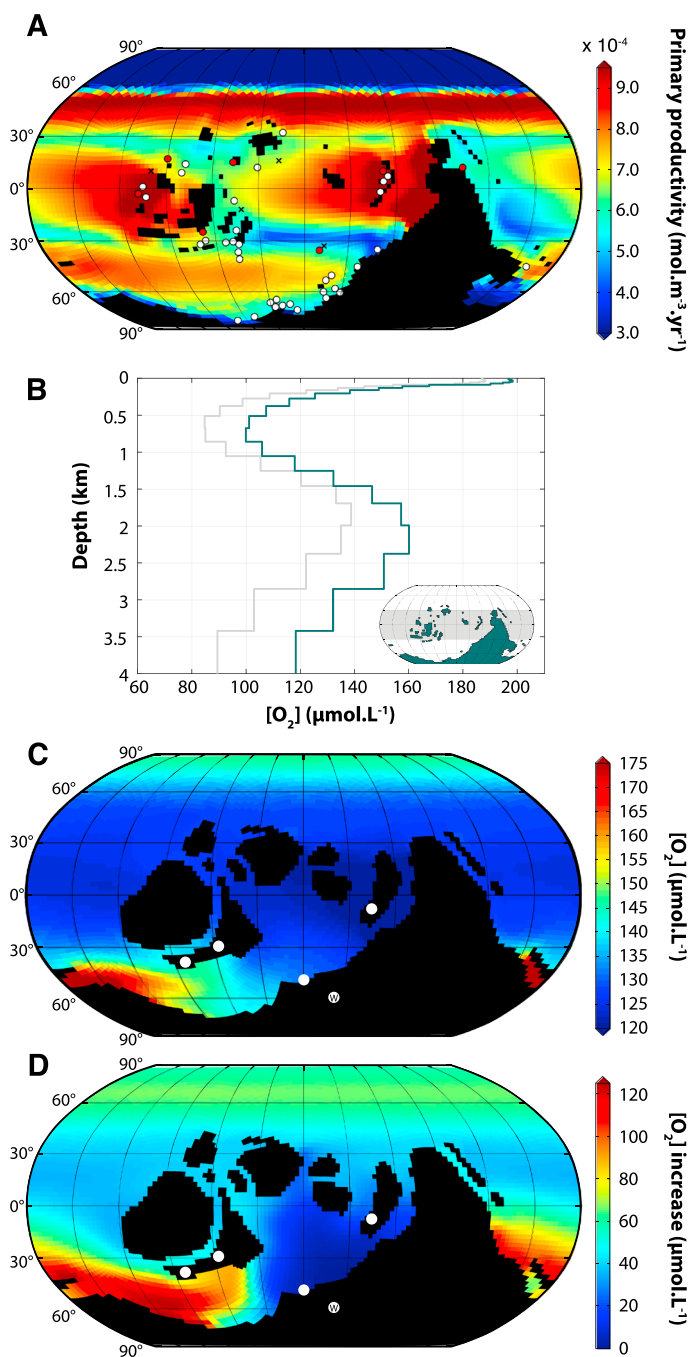


Figure 8. Impact of climate cooling on the primary productivity simulated at the ocean surface and on the oxygen concentration simulated throughout the water column. (a) Marine primary productivity simulated using the 440 Ma land-sea mask and a solar forcing level of 345 W m^{-2} . White and red dots respectively stand for sediments of Hirnantian age associated with dysoxic-to-oxic and intermittently anoxic conditions (i.e., interbedded black shales), after the compilation of Melchin *et al.* [2013]. No continuous black shale deposition is reported during the Hirnantian. See Figure S2 for data points labeling. (b) Depth profiles of mean annual, tropical oxygen concentration simulated using the 440 Ma land-sea mask and solar forcing values of 350 W m^{-2} (light grey curve) and 345 W m^{-2} (dark grey curve). The insert in the bottom right corner represents the area over which data were averaged. The plot focuses on the tropical ocean, where major shifts in redox conditions are documented from the Katian to the Hirnantian [Melchin *et al.*, 2013]. (c) Oxygen concentration simulated at the ocean bottom at 350 W m^{-2} . (d) Increase in ocean bottom oxygen concentration simulated when decreasing solar forcing from 350 W m^{-2} to 345 W m^{-2} . Please note that the increase is positive everywhere. In Figures 8c and 8d, large white dots correspond to the location of the samples of Hammarlund *et al.* [2012], Zhang *et al.* [2009], and Yan *et al.* [2009]. The location of the well used by Vandenbroucke *et al.* [2015] is identified with a “W.”

value (see section 4.3) confirm that it is difficult to reach deep-ocean anoxia during the Hirnantian (Figure S7). While most of the ocean bottom is suboxic to anoxic under Katian climatic conditions (i.e., dissolved oxygen levels below $25 \mu\text{mol L}^{-1}$), deep-ocean oxygen values stay above $25 \mu\text{mol L}^{-1}$ everywhere, except in the Paleo-Tethys, under Hirnantian conditions (i.e., solar forcing dropped to 345 W m^{-2}).

Our simulations do not account for the drop in continental weathering that should accompany climate cooling [Le Hir *et al.*, 2009; Beaulieu *et al.*, 2012]. The latter would be at least one order of magnitude higher than the $\sim 1.5\%$ decrease in PAR associated with the lower solar luminosity used to simulate Hirnantian climate, thus further reducing modeled net primary productivity and strengthening the oxygenation of the water column through decreased remineralization.

5.2. Discussion: The Hirnantian Oxygenation Event

The sediments preserved in relatively shallow environments record a worldwide shift from less oxygenated to more ventilated depositional settings during the Hirnantian [Melchin *et al.*, 2013], which is consistent with the general oxygenation trend accompanying climate cooling in our runs. The redox state of the ocean interior, however, remains the subject of hot controversy. Depending on the proxies, the Hirnantian ocean is described as undergoing vigorous sea floor oxygenation [Armstrong and Coe, 1997; Page *et al.*, 2007; LaPorte *et al.*, 2009; Zhou *et al.*, 2012; Melchin *et al.*, 2013], or deep-water anoxia [Brenchley *et al.*, 1994; Hammarlund *et al.*, 2012; Zhang *et al.*, 2009]. Such uncertainties are, at least partly, rooted in the intrinsically lacunar nature of the Early Paleozoic sedimentary record. Due to the lack of preservation of pre-Mesozoic ocean bottom sediments [Cramer and Saltzman, 2007a], deep-ocean redox conditions must be reconstructed based on ocean proxies preserved in shelf or slope settings [Hammarlund *et al.*, 2012; Melchin *et al.*, 2013]. The possibility of an Hirnantian deep-water oxygenation event [Zhou *et al.*, 2012] is supported by geochemical data. LaPorte *et al.* [2009] and Melchin *et al.* [2013] notably report a positive $\delta^{15}\text{N}$ excursion, which they interpret as a decreased contribution of cyanobacterial N fixation to the phytoplankton productivity, representative of a more oxygenated ocean during the glacial pulse. Based on the analysis of various redox proxies of the ocean, Zhou *et al.* [2012] further suggest that the Ordovician-Silurian transition is characterized by persistent basinal anoxia, with the exception of an intense oxygenation event during the Hirnantian. On the contrary, Zhang *et al.* [2009] and Hammarlund *et al.* [2012], although they agree on the oxic nature of the shallow-water deposits during the Hirnantian, document a positive excursion in the stable isotope compositions of sedimentary pyrite sulfur ($\delta^{34}\text{S}_{\text{pyr}}$) [see also Yan *et al.*, 2009], which they explain by enhanced burial rates of pyrite in the context of deep-water anoxia during the same period of time. Interestingly, Jones and Fike [2013] recently rejected this theory based on new paired sulfate-pyrite $\delta^{34}\text{S}$ data from Anticosti Island. In their geochemical record, they observe the positive enrichment in $\delta^{34}\text{S}_{\text{pyr}}$ previously reported by Hammarlund *et al.* [2012] and Zhang *et al.* [2009], but no parallel excursion in carbonate-associated sulfate ($\delta^{34}\text{S}_{\text{CAS}}$). Based on geochemical modeling, they demonstrate that an increase in pyrite burial strong enough to generate a sulfur isotope excursion during the Hirnantian would necessarily induce a parallel excursion of equal magnitude in the isotopic composition of coeval marine sulfate. The absence of such parallel excursion in their $\delta^{34}\text{S}_{\text{CAS}}$ record therefore precludes enhanced pyrite burial as the cause of the Hirnantian $\delta^{34}\text{S}_{\text{pyr}}$ excursion. Results from our general circulation model suggest that the climate cooling associated with the Hirnantian glacial pulse induces an increase in oxygen concentration throughout the water column. They support the visions of a better ventilated Hirnantian deep ocean [Melchin *et al.*, 2013; LaPorte *et al.*, 2009; Zhou *et al.*, 2012; Jones and Fike, 2013].

The hypothesis of a well-oxygenated Hirnantian ocean brings crucial insights into the mechanisms that possibly drove the turnovers in marine living communities reported for that time period. The Late Ordovician extinction is one of the “big five” mass extinctions that punctuated the Phanerozoic [Servais *et al.*, 2010], with the disappearance of about 85% of all marine species [Sheehan, 2001; Harper *et al.*, 2013a]. The coincidence of the two pulses of the extinction event with respectively the onset and demise of the Hirnantian glacial maximum suggests that these abrupt environmental changes caused the extinction [e.g., Sheehan, 2001]. The precise underlying mechanisms, however, are still a matter of debate [Luo *et al.*, 2016]. While the global spread of anoxia, in the context of the postglacial transgression, is generally admitted to explain the second pulse of the extinction [Harper *et al.*, 2013a; Melchin *et al.*, 2013; Luo *et al.*, 2016], a general consensus about the kill mechanisms implied in the first phase of the event is still lacking [Harper *et al.*, 2013a]. It is often considered that the global climate cooling and eustatic sea level fall lead to a critical habitat destruction [Sheehan, 2001]. The intensification in ocean ventilation may also have strongly stricken the fauna adapted to the preglacial sluggish ocean circulation and associated ocean water chemistry [Berry *et al.*, 1990]. Contrasting to this, however, Hammarlund *et al.* [2012] and Zhang *et al.* [2009] recently proposed the development of deep-water

anoxia as a primary kill mechanism during the first event of the faunal mass extinction. Based on the temporal correlation between the enrichment of ocean water in harmful metals (potentially under oxygen-depleted conditions) on the one hand, and high rates of plankton malformations and extinction of marine species on the other hand, *Vandenbroucke et al.* [2015] further supported the role of anoxia as a dominant kill mechanism through the Ordovician-Silurian transition. Our findings suggest that the ocean was generally better ventilated during the Hirnantian glacial event than it was before it and do not support an Hirnantian oceanic anoxic event as the primary cause for the first pulse of the Late Ordovician extinction.

We also note that some of the data on which the latter hypothesis is based come from the margins of the Paleo-Tethys. This is notably the case for the samples of *Zhang et al.* [2009], from South China, and for the Carnic Alps section of *Hammarlund et al.* [2012], which was located along the northern margin of Gondwana during the Ordovician (Figures 8c and 8d). Similarly, the metal content measurements of *Vandenbroucke et al.* [2015] were conducted on samples obtained from a well situated in the Libyan desert, on the northern margin of Gondwana, in a region that was washed by the waters from the Paleo-Tethys as well (Figures 8c and 8d). We showed that the Paleo-Tethys is characterized by a low sea floor oxygenation under a warm climate. We further demonstrated that when a cooling is applied, this region remains dynamically insulated from the global ocean. Here the increase in ocean bottom oxygen concentration is minimum. This particular Paleo-Tethysian context therefore suggests that some of the data that served to the construction of the paradigm of an Hirnantian oceanic anoxic event may be of regional significance. This hypothesis is supported by several geochemical studies demonstrating that at least some of the trace metal accumulations measured by *Vandenbroucke et al.* [2015] (Fe, Mo, Pb, Mn, Ba, and As) are recorders of local rather than global redox conditions [e.g., *Hoffman et al.*, 1998; *Algeo and Maynard*, 2008; *Och et al.*, 2015; *Owens et al.*, 2017].

6. The Early Silurian Rhuddanian Oceanic Anoxic Event

Following the mid-Hirnantian oxygenation event, the early Silurian represents the worldwide spread of anoxia [*Melchin et al.*, 2013]. While a return to a warmer climate, in the context of the Hirnantian deglaciation, may provide a valid explanation to the deposition of black shales at tropical latitudes, we have shown previously that it would not explain the preservation of organic matter-rich deposits around Baltica and over the South Pole, along the coast of Gondwana (section 4.2). This requires additional mechanisms. So far, two main theories have been proposed: (i) stratification of the water column and oxygen depletion at depth, through the input of freshwater during the melt of the Gondwana ice sheet [*Armstrong et al.*, 2005, 2009; *Melchin et al.*, 2013], and (ii) increased primary productivity fueled by the release of nutrients during the weathering of newly exposed glaciogenic sediments experiencing climate warming [*Armstrong et al.*, 2005, 2009; *Le Heron et al.*, 2013]. Below, we use our general circulation model of the ocean to test each of these hypotheses.

6.1. Impact of a Freshwater Flux

The freshwater flux associated with the melt of the Gondwana ice sheet may have significantly slowed down the formation of deep water over the South Pole, promoting water column stratification, oxygen impoverishment, and thus organic matter preservation at depth. This scenario has been proposed to explain the deposition of black shales during the early Silurian [*Armstrong et al.*, 2005, 2009; *Melchin et al.*, 2013]. It is also supported by recent studies highlighting the critical role of ocean dynamics in the ventilation of the deep ocean and thus in the likelihood that the Earth System may be affected by an oceanic anoxic event [*Donnadieu et al.*, 2016]. In models, increased freshwater fluxes to the ocean (e.g., from ice sheet melting) often result in a significant weakening of the overturning circulation. This effect can be associated with an hysteresis behavior, whereby the overturning does not fully recover once the freshwater perturbation stops [*Stommel*, 1961; *Rahmstorf*, 1996, and many others]. The impact of a freshwater flux on the Ordovician ocean circulation has never been quantified, and such hypotheses remain essentially speculative so far.

Here we build on numerous previous studies [see, e.g., *Kageyama et al.*, 2013, and references therein] to conduct, for the first time, freshwater hosing experiments in the Silurian. We restart our model from the mid-Hirnantian climatic steady state (345 W m^{-2} ; see section 5), and we run a transient simulation, by (i) imposing a freshwater perturbation for 500 years and (ii) integrating the model for 500 additional years once the freshwater perturbation stops. This allows us to investigate both the response of the ocean circulation to a meltwater pulse, the duration of which is of the same order as the abrupt events of the last glacial [*Roche et al.*, 2004], and its potential recovery, once the perturbation has come to an end. While regions of meltwater discharge have been the subject of comprehensive investigation for the last deglaciation [*Roche et al.*, 2009],

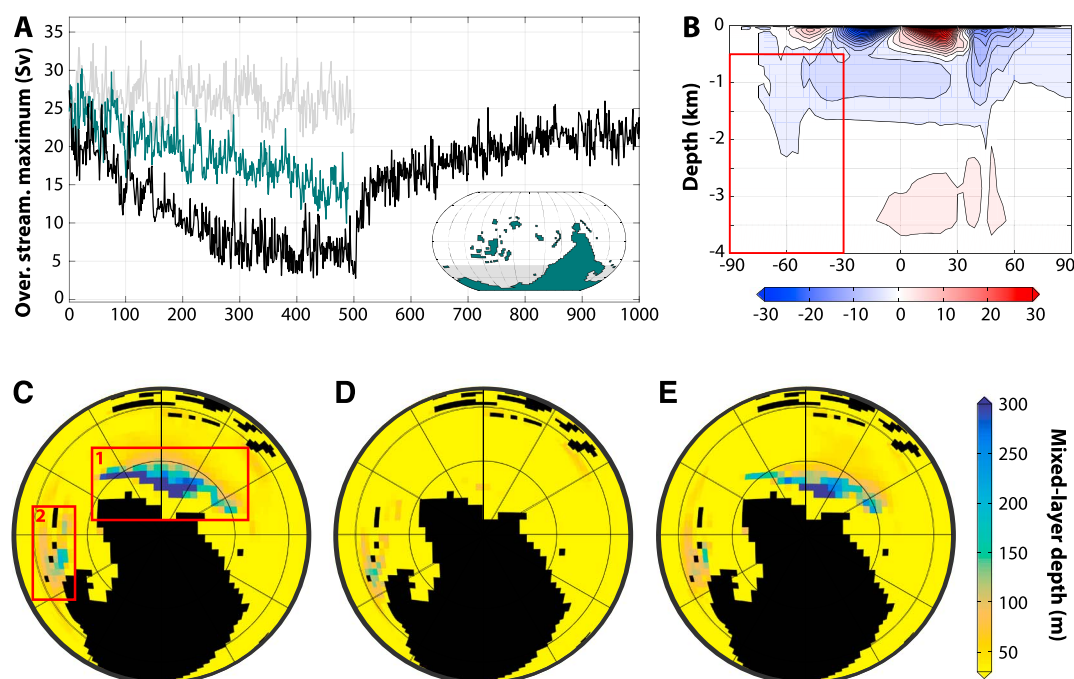


Figure 9. Results of the freshwater hosing experiments conducted at 345 W m^{-2} . (a) Evolution of the intensity of the meridional overturning stream function as a function of model integration time for three values of imposed freshwater flux: 0.1 sverdrup (Sv) (light grey line), 0.5 Sv (dark grey line), and 1 Sv (black line). The intensity of the stream function is computed, for each model year, as the maximum of the absolute value of the mean annual meridional stream function between 500 m depth and the ocean bottom, and between 90°S and 30°S (red rectangle in Figure 9b). The insert in the bottom right corner represents the area over which the freshwater flux is applied. (b) Meridional overturning stream function averaged over the years 475 to 500 of the transient simulation with a flux of 1 Sv. The contour interval is 2.5 Sv. (c) Mixed-layer depth in the unperturbed steady state (approximately year 0 in Figure 9a). (d) Mixed-layer depth averaged over the years 475 to 500 of the transient simulation with 1 Sv. (e) Mixed-layer depth averaged over the years 975 to 1000 of the transient simulation with 1 Sv.

virtually no constraints are available in the Ordovician. Freshwater can reach the open ocean at various locations, ranging from the outlet of the rivers draining the glacial watersheds to icebergs melt zones [Roche *et al.*, 2009]. Given the large uncertainties in reconstructing both the topography of Gondwana [Blakey, 2016; Scotese, 2016] and its land ice cover [Le Heron and Dowdeswell, 2009], defining zones of preferential meltwater release seems elusive. In order to simultaneously account for icebergs and coastal runoff from the Hirnantian ice sheet, which possibly reached 30°S [Torsvik and Cocks, 2013; Pohl *et al.*, 2016b], we impose a freshwater flux over a large area extending from 40°S to the South Pole (see insert in Figure 9a). We run simulations for various values of the meltwater flux: 0.1, 0.5, and 1 Sv ($1 \text{ Sv} = 10^6 \text{ m}^3 \text{ s}^{-1}$). Although they are in the range that has usually been considered in water hosing experiments about the last glacial [e.g., Prange *et al.*, 2002; Stouffer *et al.*, 2006] (see discussion in Roche *et al.* [2004]), these levels of meltwater release are 1 or 2 orders of magnitude higher than the long-term average deduced from Hirnantian land ice volume analysis. For instance, the eustatic curve reconstructed by Loi *et al.* [2010], using a backstripping procedure on the margin of Gondwana, shows a sea level increase of $\sim 70 \text{ m}$ in 70 kyr, equivalent to a meltwater flux of $\sim 0.015 \text{ Sv}$ in the Ordovician. Although sudden glacial outburst events would probably not be captured by Loi *et al.* [2010], our higher meltwater flux rate (1 Sv) is 2 orders of magnitude larger than the inferred average rate (0.015 Sv). Our simulations allow us to characterize the response (and potential recovery) of the early Silurian ocean to a weakening of the deep-water formation along the coast of Gondwana over a large range of meltwater fluxes.

Results are displayed in Figure 9a. In the initial (undisturbed by freshwater) state (i.e., year 0 in Figure 9a), two sites of particularly deep mixed layer stand out (red rectangles in Figure 9c), with deep-water formation essentially occurring along the coast of Gondwana over the South Pole (region No. 1 in Figure 9c; see also Figure 4c). When a freshwater flux is imposed, the ocean circulation weakens, from an initial maximum (in absolute value) of $\sim 25 \text{ Sv}$ to ~ 24 , 15, and 7 Sv after 500 years of perturbation with respectively 0.1, 0.5, and 1 Sv (Figure 9a). A freshwater flux of 1 Sv, in particular, leads to a significant weakening of the circulation: the mixed layer gets

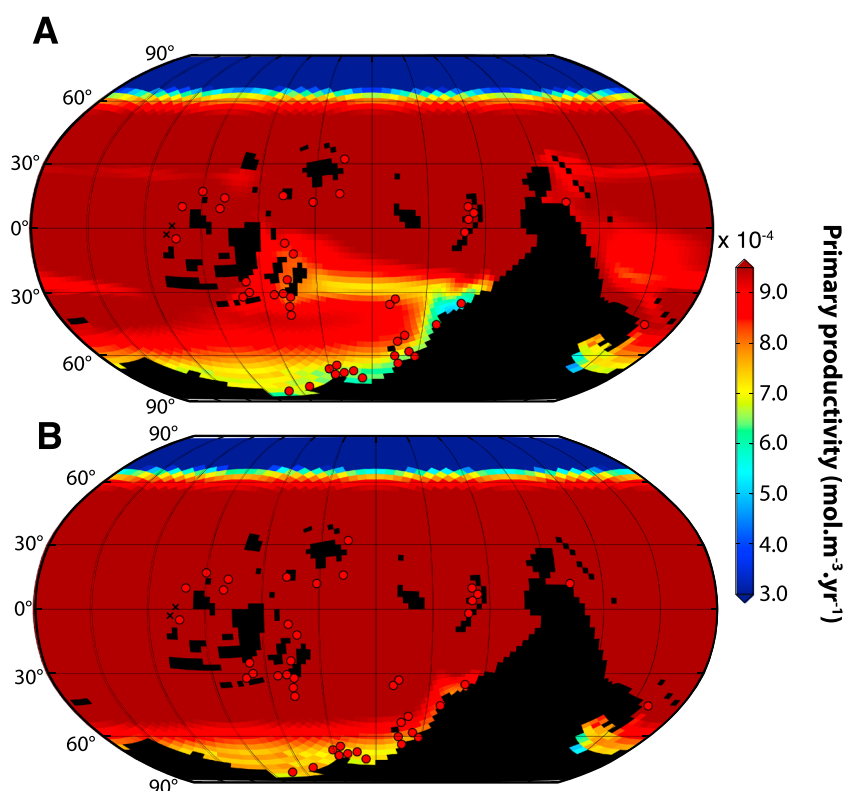


Figure 10. Surface primary productivity simulated using the 440 Ma land-sea mask, a solar forcing level of 350 W m^{-2} and an initial PO_4 depth profile defined as (a) 1.5 times the values used in the baseline runs and (b) 2 times the values used in the baseline runs. White and red dots respectively stand for sediments of early Silurian (Rhuddanian) age associated with dysoxic-to-oxic and at least intermittently anoxic conditions (i.e., interbedded black shales and black shales), after the compilation of Melchin et al. [2013]. See Figure S2 for data points labeling. Same color scale as Figure 3a.

shallower at site No. 2 and deep-water formation at site No. 1 virtually ceases (Figure 9d), as testified by the lost of the Southern Hemisphere anticlockwise cell of the overturning circulation (compare Figure 4c with Figure 9b). Elsewhere, the structure of the ocean circulation is unchanged. In particular, deep-water formation is not initiated elsewhere in response to the collapse of the Southern Hemisphere cell. When the freshwater flux is stopped the ocean circulation rapidly recovers, reaching 15 Sv after about 100 years (absolute value, see Figure 9a). After 500 years, it almost reaches its initial intensity, and the two sites of deep-water formation reappear (Figure 9e).

Previous water hosing experiments conducted under preindustrial and last glacial conditions have shown that the initial climatic state may significantly impact the sensitivity of the climate system to a release of freshwater [Ganopolski and Rahmstorf, 2001; Prange et al., 2002; Kageyama et al., 2013]. In order to assess the robustness of our results under various climatic conditions, we repeat the freshwater hosing experiments under a warmer climate (350 W m^{-2} , Figure S8) and under an abrupt climate warming potentially representative of the Silurian deglaciation (Figure S9). In both cases, the ocean circulation rapidly recovers when the release of meltwater stops.

6.2. Impact of an Increased Nutrient Supply to the Ocean

Weathering of sediments exposed in formerly glaciated regions, promoted by global climate warming, may have favored the release of nutrients from the continents during the deglaciation [Melchin et al., 2013]. This theory has been suggested in several published studies [e.g., Armstrong et al., 2005, 2009; Le Heron et al., 2013]. It is also supported by the changes in clay mineral composition documented in the Kufra basin (Libya) by Meinhold et al. [2015], who interpreted an increase in kaolinite content as probably representative of enhanced continental weathering due to the climate change occurring from the Late Ordovician icehouse to the Silurian greenhouse. Similarly, Finlay et al. [2010] demonstrated an increase in continental weathering concomitant with the deglaciation based on osmium isotope analysis. The possible diversification of nonvascular land

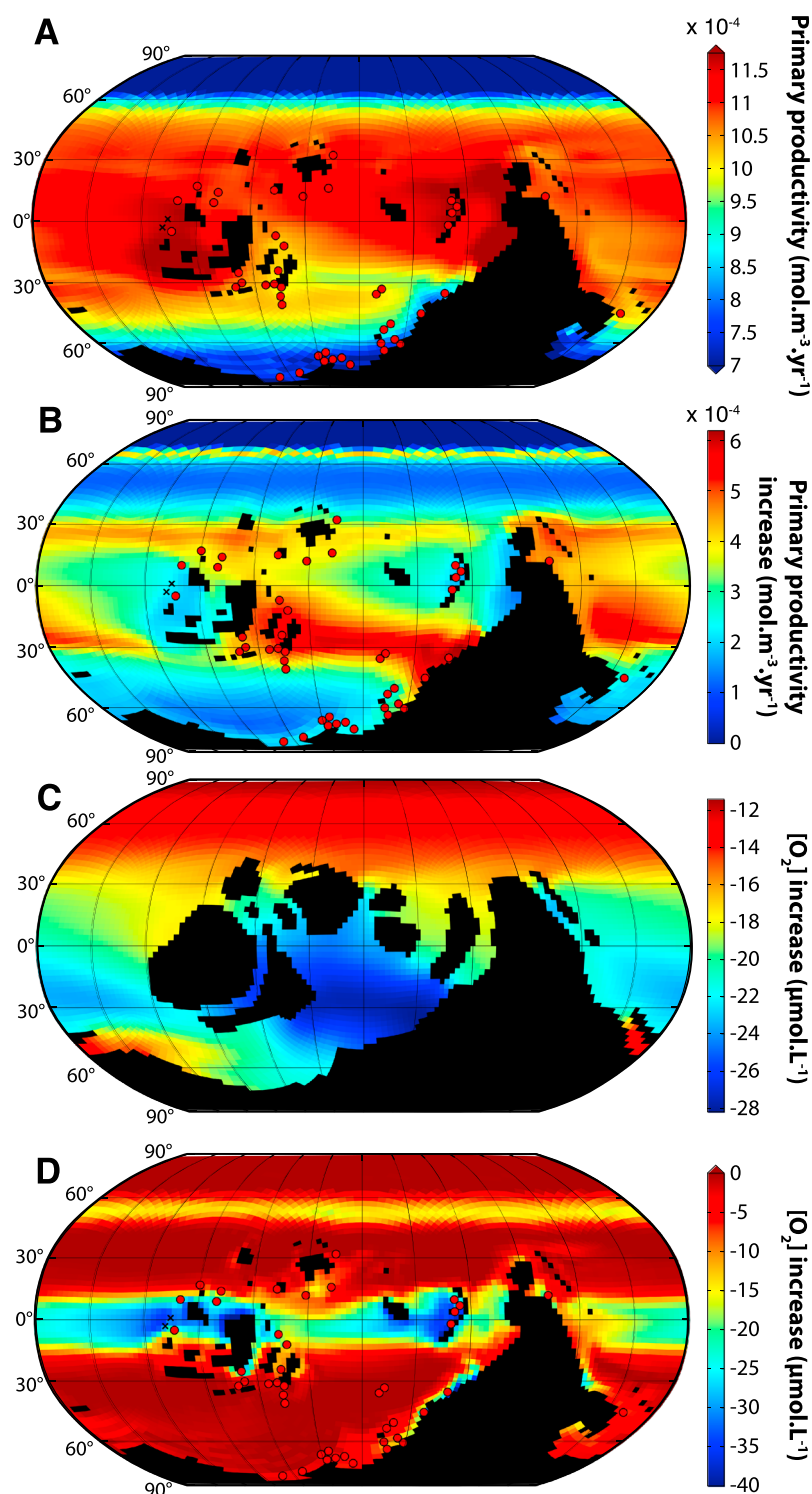


Figure 11. Impact of a doubling nutrient (PO_4) stock on the primary productivity simulated at the ocean surface, and on the oxygen concentration simulated throughout the water column. (a) Marine primary productivity simulated using the 440 Ma land-sea mask, a solar forcing level of 350 W m^{-2} and an initial PO_4 depth profile defined as twice the values used in the baseline runs. White and red dots after the compilation of Melchin *et al.* [2013]. Same as Figure 10b, with better suited color scale. (b) Increase in surface primary productivity simulated when doubling the nutrient stock in the ocean. (c) Increase in oxygen concentration simulated at the ocean bottom when doubling the initial ocean phosphate concentration. (d) Increase in oxygen concentration simulated at the depth of the epicontinental seas in the model ($\sim 80 \text{ m}$) when doubling the nutrient stock. The increase in oxygen concentration does not exceed $3.4 \mu\text{mol L}^{-1}$ anywhere.

plants during the Hirnantian [Vecoli *et al.*, 2011]—the weathering effect of which has been demonstrated [Lenton *et al.*, 2012; Porada *et al.*, 2016]—may also have constituted an additional source of nutrients to the ocean during the early Silurian deglaciation [Melchin *et al.*, 2013].

In this section, we therefore investigate the impact of an increased nutrient supply to the ocean on the marine primary productivity and oxygen concentration simulated in a warm climate (350 W m^{-2} , see section 3). A twofold increase in continental weathering flux is easily reached under a warming climate [Le Hir *et al.*, 2009; Beaulieu *et al.*, 2012]. Once anoxic conditions are established, higher phosphate content can be further sustained through phosphorus regeneration from the sediment [Van Cappellen and Ingall, 1994; Palastanga *et al.*, 2011]. A first Silurian scenario considering an intensification of the continental weathering by a factor of 1.5 shows a strong increase in net primary productivity at the global scale (Figure 10a). Levels of primary productivity allowing the deposition of black shales during the Katian (see section 4, Figure 3a in particular) are reached at all the localities reported by Melchin *et al.* [2013], except two of them found on the margin of Gondwana in the Paleo-Tethys. Based on the same criteria, a doubling nutrient supply provides a perfect model-data agreement (Figure 10b). In detail, a doubling phosphate supply does not impact the values of surface primary productivity evenly in space but induces significant changes in the spatial patterns (compare Figure 11a with Figure 3a). This is due to a large increase in the regions of previously minimum primary productivity (Figure 11b), resulting from the saturating Michaelis-Menten kinetics used in the parametrization of NPP (equation (1)). The maximal increase occurs in the area between eastern Baltica and western Gondwana, which was previously typified by oxic deposits during the Katian (Figure 11b, see section 4.1). As a consequence of the larger export of organic matter to depth, oxygen consumption by aerobic respiration gets more intense throughout the water column, and the oxygen concentration decreases in the ocean interior. At depth, the oxygen concentration decreases everywhere (Figure 11c). The latter decrease is minimum in the cold waters over the North Pole (thermal effect), and in regions of deep water convection, which benefit from the input of oxygen-rich water masses coming from the surface ocean (ocean dynamics effect). The decrease in oxygen water content is maximum in the Paleo-Tethys, that does not benefit from any of these two effects and furthermore corresponds to the region of maximum increase in surface primary productivity (Figure 11b). The impoverishment in dissolved oxygen is more moderate at the depth of the epicontinental seas because the exchange with the oxygen-rich mixed-layer waters is important (Figure 11d). The largest decrease in oxygen content occurs with the upwelling of oxygen-depleted waters from the oxygen minimum zone, at equatorial latitudes and also in place of the Panthalassic Circumpolar Current in the Northern Hemisphere (Figure 11d).

6.3. Discussion: The Nutrient-Driven Rhuddanian OAE

Two main arguments have been proposed to explain the early Rhuddanian OAE: release of meltwater, salinity stratification and enhanced preservation of organic matter, or leaching of the newly exposed glaciogenic sediments and nutrient-driven increase in marine primary productivity. We first investigated the “meltwater hypothesis” by imposing a freshwater flux over the South Pole. Our simulations show that a limited water discharge (0.1 Sv) has virtually no effect on the ocean circulation. A strong freshwater flux (0.5–1 Sv) is required to induce the collapse of the latter. Such levels of water discharge over several thousands of years cannot be realistically maintained. For comparison, such rates have been associated with the meltwater pulses of the last glacial, and only over much shorter periods [e.g., Prange *et al.*, 2002]. The question, however, remains [e.g., Melchin *et al.*, 2013, p. 1659] whether abrupt events of this kind—of a few hundred of years in duration [Roche *et al.*, 2004]—could explain the deposition of black shales for several hundred thousand years in the early Silurian [Armstrong *et al.*, 2009; Melchin *et al.*, 2013]. In our model runs, the Ordovician overturning circulation rapidly collapses when a strong (1 Sv) freshwater flux is applied over the South Pole. However, once the flux is stopped, the ocean circulation promptly recovers, in a few hundred years as well, without showing any evidence of hysteresis. Although glacial outbursts have been documented during the demise of the Hirnantian ice sheet, these events are supposed to have lasted several days to several years, with a 1–40 kyr recurrence period [Girard *et al.*, 2012]. Therefore, such short-lived and occasional meltwater pulses are no valid explanation for the protracted oxygen depletion event typifying the early Silurian ocean. We emphasize that some studies of the Last Glacial Maximum propose that under certain conditions, the overturning circulation may not recover after a meltwater perturbation [Prange *et al.*, 2002]. This is not the case in our simulations with the Ordovician continental configuration. Our results suggest that the Late Ordovician-early Silurian ocean circulation is monostable, at least in the (large) range studied here. Taken as a whole, this suggests that the meltwater flux induced by the Late Ordovician deglaciation is unable to exert a persistent effect on the ocean circulation and thus on the ocean redox state at this time. Enhanced continental weathering constitutes the

most probable driver for the Rhuddanian OAE, endorsing the visions that nutrient supply may constitute the dominant control on the spread of anoxia at various periods in the Earth's history [see *Monteiro et al.*, 2012]. Our results therefore support the theory developed by *Page et al.* [2007] regarding the long-term regulation of climate throughout the Early Paleozoic Ice Age. By favoring the sequestration of carbon in deep-sea sediments, postglacial anoxia may have drawn down atmospheric CO₂ levels and thus acted as a negative feedback mechanism preventing the onset of runaway greenhouse conditions.

However, results of water hosing experiments are model dependent [*Stouffer et al.*, 2006; *Kageyama et al.*, 2013] and additional studies, in a warm climate, are needed before drawing definitive conclusions on the mechanisms that potentially caused anoxia in the early Silurian.

7. Model Limitations and Outlook

Modeling early Paleozoic climate and marine biogeochemistry involved some degree of simplification regarding the boundary conditions and the numerical model, which potentially affected our results. We discuss these limitations below in order to highlight key points that should be investigated in follow-up studies.

7.1. Simplified Atmosphere

The main limitation of our numerical model is the highly simplified atmospheric component (SPEEDY) [*Molteni*, 2003, section 2.1]. Given that the spatial distribution of simulated primary productivity essentially arises from the wind-driven ocean mixing processes (i.e., Ekman transport, section 4.1), we pose the question: "Is our simplified atmospheric model able to correctly simulate wind stress at the surface of the Earth?" Despite the low vertical resolution of SPEEDY (five layers), the annually averaged wind stress simulated over the ocean is very similar to the one simulated using the FOAM model (Figure S10). More importantly, the pattern of simulated NPP does not depend on the details of the surface winds, but on the existence of alternating bands of winds (i.e., trades in the tropics, jet stream in the midlatitudes, and easterlies at high latitudes). This feature is extremely robust across models, suggesting that the patterns of simulated primary productivity constitute a robust result of our study.

7.2. Boundary Conditions: Radiative Forcing and Flat Bottom

Because the atmospheric component of our coupled model (SPEEDY) does not account for varying $p\text{CO}_2$ levels, we simulated different climatic states by varying the solar forcing in the model (see section 3.1). It has been demonstrated that a doubling $p\text{CO}_2$ is equivalent to an increase by $+3.7 \text{ W m}^{-2}$ in the net downward radiation at the top of the atmosphere [*Myhre et al.*, 1998]. However, it has also been shown that changes in the solar irradiance and changes in atmospheric CO₂ concentration that are equivalent from a purely radiative point of view do not produce identical climatic responses. A large part of the difference arises from the seasonal pattern of solar forcing, as opposed to greenhouse gas forcing. *Lunt et al.* [2008] and *Schmidt et al.* [2012] notably simulated significantly different patterns of precipitation and atmospheric surface temperature while trying to compensate a fourfold increase in $p\text{CO}_2$ with decreased solar input. Since precipitation (through its impact on ocean salinity) and surface temperature are the two main drivers of the oceanic overturning circulation and thus deep ocean ventilation, it would be interesting to test the impact of a more "realistic" Ordovician forcing level (i.e., decreased solar luminosity and increased $p\text{CO}_2$) [see *Herrmann et al.*, 2003, 2004; *Pohl et al.*, 2014] on the oxygenation state of the ocean throughout the Ordovician-Silurian transition.

Similarly, we have not discussed the impact of the orbital configuration on simulated climate. By changing both the spatial and temporal distribution of the solar energy received at the surface of the Earth (for a given solar constant value), the orbital configuration may also have a strong climatic impact, potentially reinforced by the powerful sea ice feedback. Unfortunately, the chaotic evolution of the orbits prevents a precise determination of the Earth motion beyond 65 Ma [*Laskar et al.*, 2004], so that no accurate orbital solution is available in the Ordovician. Future studies could address this issue through sensitivity tests to the orbital parameters (i.e., eccentricity, obliquity, and precession).

In our study, we defined the Ordovician deep-ocean bathymetry as a flat bottom. We think that this constitutes the most conservative choice because the location and depth of early Paleozoic mid-ocean ridges is essentially speculative. Nonetheless, ocean ridges may alter our results. They could block deep-ocean currents and therefore promote isolation of ocean basins while at the same time enhancing vertical mixing and topographic steering of the currents [e.g., *Gille et al.*, 2004]. These simultaneous, opposite effects make the overall ocean response difficult to predict. However, we do not think that the flat bottom constitutes a strong bias since

several modeling studies on the Permian-Triassic boundary demonstrated a minor impact of ocean ridges on both the global large-scale ocean circulation and simulated bottom oxygen concentration [Montenegro *et al.*, 2011; Osen *et al.*, 2012].

7.3. Marine Biogeochemistry

Our biogeochemistry submodel provided very new insights into the spatial distribution of primary productivity and dissolved oxygen concentration during the Ordovician. Still, some aspects of the modeling could be substantially improved.

First, no nutrient fluxes from the continent are used. A stock of phosphate is defined at the beginning of the simulation, and riverine input is not considered. A direct consequence is that the flux of freshwater to the ocean provided by continental runoff dilutes ocean water in the model and therefore leads to a decrease in net primary productivity, whereas it could theoretically promote NPP through the input of erosion-derived nutrients. Second, sedimentation is not allowed in the model, precluding any explicit diagnostic of organic matter burial. Still, we realize that coupling a sediment model with a GCM is challenging. This would require specific modeling strategies such as asynchronous coupling methods in order to deal with the very long time constant associated with the sediments.

Here we simulated the changes in the patterns of potential Late Ordovician-early Silurian marine *biomass* productivity, in response to climate changes. The Ordovician-Silurian transition, however, is also characterized by fundamental turnovers in marine living communities (i.e., *biodiversity*), which may have regionally modulated the potential for surface primary productivity [e.g., Kemp and Baldauf, 1993] and thus massive organic matter burial [e.g., Kemp *et al.*, 1999]. Following the appearance of numerous phyla during the Cambrian Explosion [e.g., Zhuravlev and Riding, 2001], the Early and Middle Ordovician record their rapid diversification, at all taxonomic levels, during the “Great Ordovician Biodiversification Event” [Webby *et al.*, 2004]. This radiation is subsequently stopped by the Late Ordovician mass extinction, when ~85% of all marine species disappear [Sheehan, 2001]. The Silurian eventually records a relatively rapid postcrisis recovery [Servais *et al.*, 2010]. The model employed in this study does not capture such variations in marine paleobiodiversity. Over the last decades, biogeochemistry models of the ocean continuously increased in complexity, by resolving more and more processes and by handling a growing number of species. Still, most up-to-date models only resolve a few phytoplankton functional types—such as diatoms, coccolithophores, and nitrogen fixers—that correspond to aggregates of many modern species characterized by common biogeochemical requirements [e.g., Aumont *et al.*, 2015]. The physiological traits of these functional types are estimated from sensing, in situ oceanic measurements, and laboratory culture experiments [Anderson, 2005]. In other words, these models are optimized for the present-day pelagic ecosystem and cannot simulate the changes of the marine biodiversity seen in deep time slices. However, recent developments in marine ecosystem models explore representations based on the principle that the community structure should self-organize, by selecting for phytoplankton with “fittest” physiological characteristics relative to surrounding environment [Litchman *et al.*, 2007; Follows *et al.*, 2007]. In this approach, tens or hundreds of phytoplankton types with various combinations of observation-based ecological strategies and physiological traits are carried in the model and allowed to compete for the available resources. Such models mimic natural selection and satisfactorily simulate the first-order patterns of present-day marine biodiversity [e.g., Barton *et al.*, 2010]. We suggest that this kind of versatile marine ecology models may constitute suitable tools to further the present, exploratory study of the coevolution of climate and the biosphere during the Early Paleozoic. This constitutes a future research target.

8. Conclusions

In this study, we employ an ocean-atmosphere setup of the MIT general circulation model (MITgcm) to investigate the changes in ocean redox state reported through the Ordovician-Silurian boundary. Our model accounts for marine primary productivity and cycling of oxygen in the ocean. We compare our modeling results with the recent black shale compilation of Melchin *et al.* [2013]. We show the following:

1. Under a warm climate representative of pre-Hirnantian times, our model does capture the spatial distribution of organic matter burial reported during the late Katian. Our results suggest that under a reduced atmospheric oxygen partial pressure and thus reduced ocean oxygen content, the deposition of black shales in the Late Ordovician may have been driven by the patterns of surface primary productivity rather than deep-ocean oxygenation. We propose that the late Katian may therefore constitute an outstanding

window into the Late Ordovician-early Silurian unperturbed oceanic redox state, and that any deviation from this should be considered as evidence of climatic perturbation or specific basinal conditions and insulation from the open ocean.

2. When a climate cooling is applied, combined effects of preferential oxygen dissolution in cold waters and enhanced oceanic overturning induce a significant oxygenation throughout the water column, providing support for an “Hirnantian oxygenation event.” These results contrast with some recent studies invoking an Hirnantian deep-water anoxic event to resolve both the positive carbon excursion reported at this time, through massive organic carbon burial, and the concomitant Late Ordovician mass extinction, through the release of toxic metals under suboxic conditions. If evidence of deep-water anoxia during the Hirnantian should be discovered in the future [Vandenbroucke *et al.*, 2015], mechanisms other than climate cooling should obviously be invoked to explain it. Such mechanisms should have a large enough effect to overcome the increased solubility.
3. In our model runs, the input of freshwater over the South Pole is not able to sustain a state of low oceanic ventilation over sufficiently long geological periods to produce the record of early Silurian anoxia. Enhanced continental weathering and nutrient input to the ocean satisfactorily account for the preferential deposition of black shales at that time.

Acknowledgments

The findings in this study are based on climatic fields simulated by the ocean-atmosphere general circulation model MITgcm. Code for the climate model MITgcm can be accessed at <http://mitgcm.org>. Requests for the climate model output can be sent to A.P. (pohl@cerege.fr) or Y.D. (donnadieu@cerege.fr). The authors acknowledge the financial support from the CNRS (INSU, action SYSTER). A.P. and Y.D. thank the CEA/CCRT for providing access to the HPC resources of TGCC under the allocation 2014-012212 made by GENCI. We thank Elise Nardin (GET, Toulouse, France) for providing the 440 Ma basemap. A.P. thanks Maura Brunetti from the University of Geneva, who provided expertise that greatly assisted the research. The authors also want to thank the two anonymous reviewers of this manuscript and associate Editor Gabe Bowen for their helpful and constructive comments and suggestions, and Ellen Thomas for editorial handling. This research was funded through a CEA PhD grant CFR. This is a contribution to the IGCP Project-591, “The Early to Middle Paleozoic Revolution” and IGCP Project-653, “The onset of the Great Ordovician Biodiversity Event”.

References

- Adcroft, A., C. Hill, and J. Marshall (1997), Representation of topography by shaved cells in a height coordinate ocean model, *Mon. Weather Rev.*, **125**, 2293–2315.
- Adcroft, A., J. M. Campin, and C. Hill (2004), Implementation of an atmosphere-ocean general circulation model on the expanded spherical cube, *Mon. Weather Rev.*, **132**, 2845–2863.
- Algeo, T. J., and E. Ingall (2007), Sedimentary C_{org} :P ratios, paleocean ventilation, and Phanerozoic atmospheric pO_2 , *Palaeogeogr. Palaeoclimatol. Palaeoecol.*, **256**(3–4), 130–155.
- Algeo, T. J., and J. B. Maynard (2008), Trace-metal covariation as a guide to water-mass conditions in ancient anoxic marine environments, *Geosphere*, **4**(5), 872–887.
- Anderson, T. R. (2005), Plankton functional type modelling: Running before we can walk?, *J. Plankton Res.*, **27**(11), 1073–1081.
- Armstrong, H. A., and A. L. Coe (1997), Deep-sea sediments record the geophysiology of the late Ordovician glaciation, *J. Geol. Soc. London*, **154**, 929–934.
- Armstrong, H. A., B. R. Turner, I. M. Makhlof, G. P. Weedon, M. Williams, A. Al Smadi, and A. Abu Salah (2005), Origin, sequence stratigraphy and depositional environment of an upper Ordovician (Hirnantian) deglacial black shale, Jordan, *Palaeogeogr. Palaeoclimatol. Palaeoecol.*, **220**(3–4), 273–289.
- Armstrong, H. A., G. D. Abbott, B. R. Turner, I. M. Makhlof, A. B. Muhammad, N. Pedentchouk, and H. Peters (2009), Black shale deposition in an Upper Ordovician–Silurian permanently stratified, peri-glacial basin, southern Jordan, *Palaeogeogr. Palaeoclimatol. Palaeoecol.*, **273**(3–4), 368–377.
- Arthur, M. A. (1979), North Atlantic Cretaceous black shales: The record at site 398 and a brief comparison with other occurrences, in *Initial Reports Deep Sea*, edited by J. C. Sibuet *et al.*, pp. 719–751, US Gov. Print. Off., Washington, D. C.
- Aumont, O., C. Ethé, A. Tagliabue, L. Bopp, and M. Gehlen (2015), PISCES-v2: An ocean biogeochemical model for carbon and ecosystem studies, *Geosci. Model Dev.*, **8**(8), 2465–2513.
- Barton, A. D., S. Dutkiewicz, G. Flierl, J. Bragg, and M. J. Follows (2010), Patterns of diversity in marine phytoplankton, *Science*, **327**(5972), 1509–1511.
- Beaulieu, E., Y. Goddérès, Y. Donnadieu, D. Labat, and C. Roelandt (2012), High sensitivity of the continental-weathering carbon dioxide sink to future climate change, *Nat. Clim. Change*, **2**(5), 346–349.
- Bergman, N. M., T. M. Lenton, and A. J. Watson (2004), COPSE: A new model of biogeochemical cycling over Phanerozoic time, *Am. J. Sci.*, **304**, 397–437.
- Berner, R. A. (2006), GEOCARBSULF: A combined model for Phanerozoic atmospheric O_2 and CO_2 , *Geochim. Cosmochim. Acta*, **70**(23), 5653–5664.
- Berner, R. A. (2009), Phanerozoic atmospheric oxygen: New results using the GEOCARBSULF model, *Am. J. Sci.*, **309**, 603–606.
- Berry, W. B. N., P. Wilde, and M. S. Quinby-Hunt (1990), Late Ordovician graptolite mass mortality and subsequent early silurian re-radiation, in *Lecture Notes in Earth Sciences*, pp. 115–123, Springer, Berlin.
- Bickert, T., J. Pätzold, C. Samtleben, and A. Munnecke (1997), Paleoenvironmental changes in the Silurian indicated by stable isotopes in brachiopod shells from Gotland, Sweden, *Geochim. Cosmochim. Acta*, **61**(13), 2717–2730.
- Blakey, R. C. (2016), Colorado Plateau Geosystems. [Available at: <http://cpgeosystems.com/>]
- Brenchley, P. J., J. D. Marshall, G. Carden, D. Robertson, D. Long, T. Meidla, L. Hints, and T. F. Anderson (1994), Bathymetric and isotopic evidence for a short-lived Late Ordovician glaciation in a greenhouse period, *Geology*, **22**(4), 295–298.
- Brenchley, P. J., G. Carden, and J. Marshall (1995), Environmental changes associated with the “first strike” of the Late Ordovician mass extinction, *Mod. Geol.*, **20**, 83–100.
- Brenchley, P. J., G. A. Carden, L. Hints, D. Kaljo, J. D. Marshall, T. Martma, T. Meidla, and J. Nölvak (2003), High-resolution stable isotope stratigraphy of Upper Ordovician sequences: Constraints on the timing of bioevents and environmental changes associated with mass extinction and glaciation, *Geol. Soc. Am. Bull.*, **115**(1), 89–104.
- Brunetti, M., C. Vêrard, and P. O. Baumgartner (2015), Modeling the Middle Jurassic ocean circulation, *J. Palaeogeogr.*, **4**(4), 371–383.
- Bryant, R. G. (2013), Recent advances in our understanding of dust source emission processes, *Prog. Phys. Geog.*, **37**(3), 397–421.
- Came, R. E., J. M. Eiler, J. Veizer, K. Azmy, U. Brand, and C. R. Weidman (2007), Coupling of surface temperatures and atmospheric CO_2 concentrations during the Palaeozoic era, *Nature*, **449**, 198–202.
- Chaloner, W. G. (1989), Fossil charcoal as an indicator of palaeoatmospheric oxygen level, *J. Geol. Soc.*, **146**(1), 171–174.
- Cocks, L. R. M., and T. H. Torsvik (2005), Baltica from the late Precambrian to mid-Palaeozoic times: The gain and loss of a terrane’s identity, *Earth Sci. Rev.*, **72**(1–2), 39–66.

- Cocks, L. R. M., and T. H. Torsvik (2007), Siberia, the wandering northern terrane, and its changing geography through the Palaeozoic, *Earth Sci. Rev.*, **82**(1–2), 29–74.
- Cocks, L. R. M., and T. H. Torsvik (2011), The Palaeozoic geography of Laurentia and western Laurussia: A stable craton with mobile margins, *Earth Sci. Rev.*, **106**(1–2), 1–51.
- Cocks, L. R. M., and T. H. Torsvik (2013), The dynamic evolution of the Palaeozoic geography of eastern Asia, *Earth Sci. Rev.*, **117**, 40–79.
- Cramer, B. D., and M. R. Saltzman (2005), Sequestration of ^{12}C in the deep ocean during the early Wenlock (Silurian) positive carbon isotope excursion, *Palaeogeogr. Palaeoclimatol. Palaeoecol.*, **219**(3–4), 333–349.
- Cramer, B. D., and M. R. Saltzman (2007a), Fluctuations in epeiric sea carbonate production during Silurian positive carbon isotope excursions: A review of proposed paleoceanographic models, *Palaeogeogr. Palaeoclimatol. Palaeoecol.*, **245**(1–2), 37–45.
- Cramer, B. D., and M. R. Saltzman (2007b), Early Silurian paired $\delta^{13}\text{C}_{\text{carb}}$ and $\delta^{13}\text{C}_{\text{org}}$ analyses from the Midcontinent of North America: Implications for paleoceanography and paleoclimate, *Palaeogeogr. Palaeoclimatol. Palaeoecol.*, **256**(3–4), 195–203.
- Denis, M., J.-F. Buoncristiani, M. Konaté, J.-F. Ghienne, and M. Guiraud (2007), Hirnantian glacial and deglacial record in SW Djado Basin (NE Niger), *Geodinamica Acta*, **20**(3), 177–195.
- Donnadieu, Y., E. Pucéat, M. Moiroud, F. Guillocheau, and J.-F. Deconinck (2016), A better-ventilated ocean triggered by Late Cretaceous changes in continental configuration, *Nat. Commun.*, **7**, 10316.
- Dutkiewicz, S., M. J. Follows, and P. Parekh (2005), Interactions of the iron and phosphorus cycles: A three-dimensional model study, *Global Biogeochem. Cycles*, **19**, GB1021, doi:10.1029/2004GB002342.
- Edwards, D., L. Cherns, and J. A. Raven (2015), Could land-based early photosynthesizing ecosystems have bioengineered the planet in mid-Palaeozoic times?, *Palaeontology*, **58**(5), 803–837.
- Ekman, V. W. (1905), On the influence of the Earth's rotation on ocean currents, *Ark. Mat. Astron. Fys.*, **2**, 1–53.
- Enderton, D. (2009), On the meridional heat transport and its partition between the atmosphere and oceans, PhD thesis, Massachusetts Institute of Technology.
- Enderton, D., and J. Marshall (2009), Explorations of atmosphere–ocean–ice climates on an aquaplanet and their meridional energy transports, *J. Atmos. Sci.*, **66**(6), 1593–1611.
- Falkowski, P. (2012), Ocean science: The power of plankton, *Nature*, **483**(7387), S17–S20.
- Ferreira, D., J. Marshall, and J.-M. Campin (2010), Localization of deep water formation: Role of atmospheric moisture transport and geometrical constraints on ocean circulation, *J. Clim.*, **23**(6), 1456–1476.
- Ferreira, D., J. Marshall, and B. Rose (2011), Climate determinism revisited: Multiple equilibria in a complex climate model, *J. Clim.*, **24**(4), 992–1012.
- Finlay, A. J., D. Selby, and D. R. Gröcke (2010), Tracking the Hirnantian glaciation using Os isotopes, *Earth Planetary Sci. Lett.*, **293**(3–4), 339–348.
- Finnegan, S., K. Bergmann, J. M. Eiler, D. S. Jones, D. A. Fike, I. Eisenman, N. C. Hughes, A. K. Tripathi, and W. W. Fischer (2011), The magnitude and duration of Late Ordovician–Early Silurian glaciation, *Science*, **331**(6019), 903–906.
- Finney, S. C., W. Berry, J. D. Cooper, and R. L. Ripperdan (1999), Late Ordovician mass extinction: A new perspective from stratigraphic sections in central Nevada, *Geology*, **27**(3), 215–218.
- Follows, M. J., S. Dutkiewicz, S. Grant, and S. W. Chisholm (2007), Emergent biogeography of microbial communities in a model ocean, *Science*, **315**(5820), 1843–1846.
- Friis, K., R. G. Najjar, M. J. Follows, and S. Dutkiewicz (2006), Possible overestimation of shallow-depth calcium carbonate dissolution in the ocean, *Global Biogeochem. Cycles*, **20**, GB4019, doi:10.1029/2006GB002727.
- Friis, K., R. G. Najjar, M. J. Follows, S. Dutkiewicz, A. Körtzinger, and M. Johnson (2007), Dissolution of calcium carbonate: Observations and model results in the subpolar North Atlantic, *Biogeosciences*, **4**, 205–213.
- Ganopolski, A., and S. Rahmstorf (2001), Rapid changes of glacial climate simulated in a coupled climate model, *Nature*, **409**(6817), 153–158.
- Garcia, H. E., and L. I. Gordon (1992), Oxygen solubility in seawater: Better fitting equations, *Limnol. Oceanogr.*, **37**(6), 1307–1312.
- Gent, P. R., and J. C. McWilliams (1990), Isopycnal mixing in ocean circulation models, *J. Phys. Oceanogr.*, **20**, 150–155.
- Ghienne, J.-F., D. P. Le Heron, J. Moreau, M. Denis, and M. Deynoux (2007), The Late Ordovician glacial sedimentary system of the North Gondwana platform, in *Glacial Sedimentary Processes and Products, Special Publication*, edited by M. Hambrey et al., pp. 295–319, International Association of Sedimentologists, Blackwells, Oxford.
- Gille, S. T., E. J. Metzger, and R. Tokmakian (2004), Seafloor topography and ocean circulation, *Oceanography*, **17**(1), 47–54.
- Girard, F., J.-F. Ghienne, and J.-L. Rubino (2012), Occurrence of hyperpycnal flows and hybrid event beds related to glacial outburst events in a Late Ordovician proglacial delta (Murzuq Basin, SW Libya), *J. Sediment. Res.*, **82**(9), 688–708.
- Hammarlund, E. U., T. W. Dahl, D. A. T. Harper, D. P. G. Bond, A. T. Nielsen, C. J. Bjerrum, N. H. Schovbo, H. P. Schönlaub, J. A. Zalasiewicz, and D. E. Canfield (2012), A sulfidic driver for the end-Ordovician mass extinction, *Earth Planet. Sci. Lett.*, **331**–332, 128–139.
- Hag, B. U., and S. R. Schutter (2008), A chronology of Paleozoic sea-level changes, *Science*, **322**(5898), 64–68.
- Harper, D. A. T., E. U. Hammarlund, and C. M. Ø. Rasmussen (2013a), End Ordovician extinctions: A coincidence of causes, *Gondwana Res.*, **25**(4), 1294–1307.
- Harper, D. A. T., C. M. Ø. Rasmussen, M. Liljeroth, R. B. Blodgett, Y. Candela, J. Jin, I. G. Percival, J. Y. Rong, E. Villas, and R. B. Zhan (2013b), Biodiversity, biogeography and phylogeography of Ordovician rhynchonelliform brachiopods, in *Early Palaeozoic Biogeography and Palaeogeography*, edited by D. A. T. Harper and T. Servais, pp. 127–144, Geological Society of London, Memoirs.
- Heckman, D. S., D. M. Geiser, B. R. Eidell, and R. L. Stauffer (2001), Molecular evidence for the early colonization of land by fungi and plants, *Science*, **293**, 1129–1133.
- Herrmann, A. D., M. E. Patzkowsky, and D. Pollard (2003), Obliquity forcing with 8–12 times preindustrial levels of atmospheric pCO_2 during the Late Ordovician glaciation, *Geology*, **31**(6), 485–488.
- Herrmann, A. D., B. J. Haupt, M. E. Patzkowsky, D. Seidov, and R. L. Slingerland (2004), Response of Late Ordovician paleoceanography to changes in sea level, continental drift, and atmospheric pCO_2 : Potential causes for long-term cooling and glaciation, *Palaeogeogr. Palaeoclimatol. Palaeoecol.*, **210**(2–4), 385–401.
- Hoffman, D. L., T. J. Algeo, J. B. Maynard, M. M. Joachimski, J. C. Hower, and J. Jaminski (1998), Regional and stratigraphic variation in bottomwater anoxia in offshore core shales of Upper Pennsylvanian cyclothems from the Eastern Midcontinent Shelf (Kansas), U.S.A., in *Shales and Mudstones I*, edited by J. Schieber, pp. 243–269, Schweizerbart'sche Verlagsbuchhandlung, Stuttgart.
- Jacob, R. L. (1997), Low frequency variability in a simulated atmosphere ocean system, PhD thesis, Univ. of Wisconsin-Madison.
- Jenkyns, H. C. (2010), Geochemistry of oceanic anoxic events, *Geochem. Geophys. Geosyst.*, **11**(3), Q03004.
- Jeppsson, L. (1990), An oceanic model for lithological and faunal changes tested on the Silurian record, *J. Geol. Soc.*, **147**(4), 663–674.
- Johnson, M. E. (2006), Relationship of Silurian sea-level fluctuations to oceanic episodes and events, *GFF*, **128**(2), 115–121.

- Jones, D. S., and D. A. Fike (2013), Dynamic sulfur and carbon cycling through the end-Ordovician extinction revealed by paired sulfate–pyrite $\delta^{34}\text{S}$, *Earth Planet. Sci. Lett.*, **363**, 144–155.
- Kageyama, M., et al. (2013), Climatic impacts of fresh water hosing under Last Glacial Maximum conditions: A multi-model study, *Clim. Past*, **9**(2), 935–953.
- Kaljo, D., T. Martma, P. Männik, and V. Viira (2003), Implications of Gondwana glaciations in the Baltic late Ordovician and Silurian and a carbon isotopic test of environmental cyclicity, *Bull. de la Soc. Géol. de France*, **174**(1), 59–66.
- Kemp, A., and J. G. Baldauf (1993), Vast Neogene laminated diatom mat deposits from the eastern equatorial Pacific Ocean, *Nature*, **362**, 141–144.
- Kemp, A., R. B. Pearce, I. Koizumi, J. Pike, and S. J. Rance (1999), The role of mat-forming diatoms in the formation of Mediterranean sapropels, *Nature*, **399**, 57–60.
- Kump, L. R., M. A. Arthur, M. E. Patzkowsky, M. T. Gibbs, D. S. Pinkus, and P. M. Sheehan (1999), A weathering hypothesis for glaciation at high atmospheric pCO_2 during the Late Ordovician, *Palaeogeogr. Palaeoclimatol. Palaeoecol.*, **152**(1), 173–187.
- LaPorte, D. F., C. Holmden, W. P. Patterson, J. D. Loxton, M. J. Melchin, C. E. Mitchell, S. C. Finney, and H. D. Sheets (2009), Local and global perspectives on carbon and nitrogen cycling during the Hirnantian glaciation, *Palaeogeogr. Palaeoclimatol. Palaeoecol.*, **276**(1–4), 182–195.
- Large, W. G., J. C. McWilliams, and S. C. Doney (1994), Oceanic vertical mixing: A review and a model with a nonlocal boundary layer parameterization, *Rev. Geophys.*, **32**(4), 363–403.
- Laskar, J., P. Robutel, F. Joutel, M. Gastineau, A. Correia, and B. Levrard (2004), A long-term numerical solution for the insolation quantities of the Earth, *Astron. Astrophys.*, **428**(1), 261–285.
- Le Heron, D. P., and J. Craig (2008), First-order reconstructions of a Late Ordovician Saharan ice sheet, *J. Geol. Soc. London*, **165**, 19–29.
- Le Heron, D. P., and J. A. Dowdeswell (2009), Calculating ice volumes and ice flux to constrain the dimensions of a 440 Ma North African ice sheet, *J. Geol. Soc.*, **166**(2), 277–281.
- Le Heron, D. P., J. Craig, and J. L. Etienne (2009), Ancient glaciations and hydrocarbon accumulations in North Africa and the Middle East, *Earth Sci. Rev.*, **93**(3–4), 47–76.
- Le Heron, D. P., G. Meinhold, A. Page, and A. Whitham (2013), Did lingering ice sheets moderate anoxia in the Early Palaeozoic of Libya?, *J. Geol. Soc.*, **170**(2), 327–339.
- Le Hir, G., Y. Donnadieu, Y. Goddérès, R. T. Pierrehumbert, G. P. Halverson, M. Macouin, A. Nédélec, and G. Ramstein (2009), The snowball Earth aftermath: Exploring the limits of continental weathering processes, *Earth Planet. Sci. Lett.*, **277**(3–4), 453–463.
- Lenton, T. M., M. Crouch, M. Johnson, N. Pires, and L. Dolan (2012), First plants cooled the Ordovician, *Nat. Geosci.*, **5**(2), 86–89.
- Lenton, T. M., T. W. Dahl, S. J. Daines, B. J. W. Mills, K. Ozaki, M. R. Saltzman, and P. Porada (2016), Earliest land plants created modern levels of atmospheric oxygen, *Proc. Natl. Acad. Sci. U.S.A.*, **113**(35), 9704–9709.
- Litchman, E., C. A. Klausmeier, O. M. Schofield, and P. G. Falkowski (2007), The role of functional traits and trade-offs in structuring phytoplankton communities: Scaling from cellular to ecosystem level, *Ecol. Lett.*, **10**(12), 1170–1181.
- Loi, A., et al. (2010), The Late Ordovician glacio-eustatic record from a high-latitude storm-dominated shelf succession: The Bou Ingarf section (Anti-Atlas, Southern Morocco), *Palaeogeogr. Palaeoclimatol. Palaeoecol.*, **296**(3–4), 332–358.
- Long, D. (1993), Oxygen and carbon isotopes and event stratigraphy near the Ordovician–Silurian boundary, Anticosti Island Quebec, *Palaeogeogr. Palaeoclimatol. Palaeoecol.*, **104**, 49–59.
- Loydell, D. K. (2007), Early Silurian positive $\delta^{13}\text{C}$ excursions and their relationship to glaciations, sea-level changes and extinction events, *Geol. J.*, **42**(5), 531–546.
- Loydell, D. K. (2008), Reply to ‘Early Silurian positive $\delta^{13}\text{C}$ excursions and their relationship to glaciations, sea-level changes and extinction events: discussion’ by Bradley D. Cramer and Axel Munnecke, *Geol. J.*, **43**(4), 511–515.
- Lunt, D. J., A. Ridgwell, P. J. Valdes, and A. Seale (2008), “Sunshade World”: A fully coupled GCM evaluation of the climatic impacts of geoengineering, *Geophys. Res. Lett.*, **35**, L12710, doi:10.1029/2008GL033674.
- Luo, G., T. J. Algeo, R. Zhan, D. Yan, J. Huang, J. Liu, and S. Xie (2016), Perturbation of the marine nitrogen cycle during the Late Ordovician glaciation and mass extinction, *Palaeogeogr. Palaeoclimatol. Palaeoecol.*, **448**, 339–348.
- Marshall, J., and K. Speer (2012), Closure of the meridional overturning circulation through Southern Ocean upwelling, *Nat. Geosci.*, **5**(3), 171–180.
- Marshall, J., A. Adcroft, C. Hill, L. Perelman, and C. Heisey (1997a), A finite-volume, incompressible Navier Stokes model for studies of the ocean on parallel computers, *J. Geophys. Res.*, **102**(C3), 5753–5766.
- Marshall, J., C. Hill, L. Perelman, and A. Adcroft (1997b), Hydrostatic, quasi-hydrostatic, and nonhydrostatic ocean modeling, *J. Geophys. Res.*, **102**(C3), 5733–5752.
- Marshall, J., A. Adcroft, J. M. Campin, C. Hill, and A. White (2004), Atmosphere-ocean modeling exploiting fluid isomorphisms, *Mon. Weather Rev.*, **132**, 2882–2894.
- Marshall, J., D. Ferreira, J. M. Campin, and D. Enderton (2007), Mean climate and variability of the atmosphere and ocean on an aquaplanet, *J. Atmos. Sci.*, **64**(12), 4270–4286.
- Martin, J. H., G. A. Knauer, D. M. Karl, and W. W. Broenkow (1987), VERTEX: Carbon cycling in the northeast Pacific, *Deep Sea Res.*, **34**(2), 267–285.
- McKinley, G. A., M. J. Follows, and J. Marshall (2004), Mechanisms of air-sea CO_2 flux variability in the equatorial Pacific and the North Atlantic, *Global Biogeochem. Cycles*, **18**(2), GB2011.
- Meinhold, G., D. P. Le Heron, M. Elgady, and Y. Abutarruma (2015), The search for ‘hot shales’ in the western Kufra Basin, Libya: geochemical and mineralogical characterisation of outcrops, and insights into latest Ordovician climate, *Arabian J. Geosci.*, **9**(1), 1–15.
- Melchin, M. J., C. E. Mitchell, C. Holmden, and P. Storch (2013), Environmental changes in the Late Ordovician-early Silurian: Review and new insights from black shales and nitrogen isotopes, *Geol. Soc. Am. Bull.*, **125**(11–12), 1635–1670.
- Molteni, F. (2003), Atmospheric simulations using a GCM with simplified physical parametrizations. I: Model climatology and variability in multi-decadal experiments, *Clim. Dyn.*, **20**(2–3), 175–191.
- Monteiro, F. M., R. D. Pancost, A. Ridgwell, and Y. Donnadieu (2012), Nutrients as the dominant control on the spread of anoxia and euxinia across the Cenomanian-Turonian oceanic anoxic event (OAE2): Model-data comparison, *Paleoceanography*, **27**(4), PA4209.
- Montenegro, A., P. Spence, K. J. Meissner, M. Eby, M. J. Melchin, and S. T. Johnston (2011), Climate simulations of the Permian-Triassic boundary: Ocean acidification and the extinction event, *Paleoceanography*, **26**(3), PA3207.
- Moreau, J. (2011), The late ordovician deglaciation sequence of the SW Murzuq Basin (Libya), *Basin Res.*, **23**(4), 449–477.
- Munnecke, A., M. Calner, D. A. T. Harper, and T. Servais (2010), Ordovician and Silurian sea–water chemistry, sea level, and climate: A synopsis, *Palaeogeogr. Palaeoclimatol. Palaeoecol.*, **296**(3–4), 389–413.

- Myhre, G., E. J. Highwood, K. P. Shine, and F. Stordal (1998), New estimates of radiative forcing due to well mixed greenhouse gases, *Geophys. Res. Lett.*, *25*(14), 2715–2718.
- Nardin, E., Y. Godd  ris, Y. Donnadieu, G. Le Hir, R. C. Blakey, E. Puc  at, and M. Aretz (2011), Modeling the early Paleozoic long-term climatic trend, *Geol. Soc. Am. Bull.*, *123*(5–6), 1181–1192.
- Och, L. M., et al. (2015), Palaeoceanographic controls on spatial redox distribution over the Yangtze Platform during the Ediacaran–Cambrian transition, *Sedimentology*, *63*(2), 378–410.
- Osen, A. K., A. M. E. Winguth, C. Winguth, and C. R. Scotese (2012), Sensitivity of Late Permian climate to bathymetric features and implications for the mass extinction, *Global Planet. Change*, 171–179.
- Owens, J. D., T. W. Lyons, D. S. Hardisty, C. M. Lowery, Z. Lu, B. Lee, and H. C. Jenkyns (2017), Patterns of local and global redox variability during the Cenomanian–Turonian Boundary Event (Oceanic Anoxic Event 2) recorded in carbonates and shales from central Italy, *Sedimentology*, *64*(1), 168–185.
- Page, A., J. A. Zalasiewicz, M. Williams, and L. E. Popov (2007), Were transgressive black shales a negative feedback modulating glacioeustasy in the Early Palaeozoic Icehouse?, in *Deep-Time Perspectives on Climate Change: Marrying the Signal from Computer Models and Biological Proxies*, edited by M. Williams et al., pp. 123–156, The Micropalaeontological Society, Special Publications, The Geological Society, London.
- Palastanga, V., C. P. Slomp, and C. Heinze (2011), Long-term controls on ocean phosphorus and oxygen in a global biogeochemical model, *Global Biogeochem. Cycles*, *25*, GB3024, doi:10.1029/2010GB003827.
- Pohl, A., Y. Donnadieu, G. Le Hir, J. F. Buoncristiani, and E. Vennin (2014), Effect of the Ordovician paleogeography on the (in)stability of the climate, *Clim. Past*, *10*(6), 2053–2066.
- Pohl, A., E. Nardin, T. Vandenbroucke, and Y. Donnadieu (2016a), High dependence of Ordovician ocean surface circulation on atmospheric CO₂ levels, *Palaeogeogr. Palaeoclimatol. Palaeoecol.*, *458*, 39–51.
- Pohl, A., Y. Donnadieu, G. Le Hir, J. B. Ladant, C. Dumas, J. Alvarez-Solas, and T. R. A. Vandenbroucke (2016b), Glacial onset predated Late Ordovician climate cooling, *Paleoceanography*, *31*, 800–821.
- Porada, P., T. M. Lenton, A. Pohl, B. Weber, L. Mander, Y. Donnadieu, C. Beer, U. P  schl, and A. Kleidon (2016), High potential for weathering and climate effects of non-vascular vegetation in the Late Ordovician, *Nat. Commun.*, *7*, 12113.
- Poulsen, C. J., C. Tabor, and J. D. White (2015), Long-term climate forcing by atmospheric oxygen concentrations, *Science*, *348*(6240), 1238–1241.
- Poussart, P. F., A. J. Weaver, and C. R. Barnes (1999), Late Ordovician glaciation under high atmospheric CO₂: A coupled model analysis, *Paleoceanography*, *14*(4), 542–558.
- Prange, M., V. Romanova, and G. Lohmann (2002), The glacial thermohaline circulation: Stable or unstable?, *Geophys. Res. Lett.*, *29*(21), 2028, doi:10.1029/2002GL015337.
- R Core Team (2013), *R: A Language and Environment for Statistical Computing*, R Foundation for Statistical Computing, Vienna, Austria.
- Rahmstorf, S. (1996), On the freshwater forcing and transport of the Atlantic thermohaline circulation, *Clim. Dyn.*, *12*, 799–811.
- Rasmussen, C. M.   ., and D. A. T. Harper (2011), Did the amalgamation of continents drive the end Ordovician mass extinctions?, *Palaeogeogr. Palaeoclimatol. Palaeoecol.*, *311*(1–2), 48–62.
- Redi, M. H. (1982), Oceanic isopycnal mixing by coordinate rotation, *J. Phys. Oceanogr.*, *12*, 1154–1158.
- Roche, D., D. Paillard, and E. Cortijo (2004), Constraints on the duration and freshwater release of Heinrich event 4 through isotope modelling, *Nature*, *432*(7015), 379–382.
- Roche, D. M., A. P. Wiersma, and H. Renssen (2009), A systematic study of the impact of freshwater pulses with respect to different geographical locations, *Clim. Dyn.*, *34*(7–8), 997–1013.
- Rose, B. E. J., and J. Marshall (2009), Ocean heat transport, sea ice, and multiple climate states: Insights from energy balance models, *J. Atmos. Sci.*, *66*(9), 2828–2843.
- Rubinstein, C. V., P. Gerrienne, G. S. de la Puente, R. A. Astini, and P. Steemans (2010), Early Middle Ordovician evidence for land plants in Argentina (eastern Gondwana), *New Phytol.*, *188*(2), 365–369.
- Ruttenberg, K. C. (1993), Reassessment of the oceanic residence time of phosphorus, *Chem. Geol.*, *107*, 405–409.
- Sageman, B. B., S. R. Meyers, and M. A. Arthur (2006), Orbital time scale and new C-isotope record for Cenomanian–Turonian boundary stratotype, *Geology*, *34*(2), 125–128.
- Schlanger, S. O., and H. C. Jenkyns (2007), Cretaceous oceanic anoxic events: Causes and consequences, *Geol. Mijnbouw*, *55*(4–3), 179–184.
- Schmidt, H., et al. (2012), Solar irradiance reduction to counteract radiative forcing from a quadrupling of CO₂: Climate responses simulated by four earth system models, *Earth Syst. Dyn.*, *3*(1), 63–78.
- Scotese, C. R. (2016), PALEOMAP project. [Available at: <http://www.scotese.com>.]
- Servais, T., A. W. Owen, D. A. Harper, B. Kr  ger, and A. Munnecke (2010), The Great Ordovician Biodiversification Event (GOBE): The palaeoecological dimension, *Palaeogeogr. Palaeoclimatol. Palaeoecol.*, *294*(3), 99–119.
- Servais, T., T. Danelian, D. A. T. Harper, and A. Munnecke (2014), Possible oceanic circulation patterns, surface water currents and upwelling zones in the Early Palaeozoic, *GFF*, *136*(1), 229–233.
- Sheehan, P. M. (2001), The late Ordovician mass extinction, *Annu. Rev. Earth Planet. Sci.*, *29*(1), 331–364.
- Steenmans, P., A. Le Heriss  , J. Melvin, M. A. Miller, F. Paris, J. Verniers, and C. H. Wellman (2009), Origin and radiation of the earliest vascular land plants, *Science*, *324*(5925), 353–353.
- Stommel, H. (1961), Thermohaline convection with two stable regimes of flow, *Tellus*, *13*(2), 224–230.
- Stouffer, R. J., et al. (2006), Investigating the causes of the response of the thermohaline circulation to past and future climate changes, *J. Clim.*, *19*, 1365–1387.
- Sutcliffe, O. E., J. A. Dowdeswell, R. J. Whittington, J. N. Theron, and J. Craig (2000), Calibrating the Late Ordovician glaciation and mass extinction by the eccentricity cycles of Earth’s orbit, *Geology*, *28*(11), 967–970.
- Torsvik, T. H., and L. R. M. Cocks (2009), BugPlates: Linking biogeography and palaeogeography, software manual. [Available at: <http://www.geodynamics.no/bugs/SoftwareManual.pdf>.]
- Torsvik, T. H., and L. R. M. Cocks (2013), Gondwana from top to base in space and time, *Gondwana Res.*, *24*(3–4), 999–1030.
- Trabucho-Alexandre, J., W. W. Hay, and P. L. De Boer (2012), Phanerozoic environments of black shale deposition and the Wilson Cycle, *Solid Earth*, *3*(1), 29–42.
- Trotter, J. A., I. S. Williams, C. R. Barnes, C. L  cuyer, and R. S. Nicoll (2008), Did cooling oceans trigger Ordovician biodiversification? Evidence from conodont thermometry, *Science*, *321*, 550–554.
- Trotter, J. A., I. S. Williams, C. R. Barnes, P. M  nnik, and A. Simpson (2016), New conodont   ¹⁸O records of Silurian climate change: Implications for environmental and biological events, *Palaeogeogr. Palaeoclimatol. Palaeoecol.*, *443*, 34–48.

- Tukey, J. W. (1977), *Exploratory Data Analysis* 1edn., Addison-Wesley series in behavioral science, Addison-Wesley Publ. Company, Reading, Mass.
- Van Cappellen, P., and E. D. Ingall (1994), Benthic phosphorus regeneration, net primary production, and ocean anoxia: A model of the coupled marine biogeochemical cycles of carbon and phosphorus, *Paleoceanography*, 9(5), 677–692.
- Vandenbroucke, T. R. A., P. Emsbo, A. Munnecke, N. Nuns, L. Duponchel, K. Lepot, M. Quijada, F. Paris, T. Servais, and W. Kiessling (2015), Metal-induced malformations in early Palaeozoic plankton are harbingers of mass extinction, *Nature Commun.*, 6, 7966.
- Vecoli, M., A. Delabroye, A. Spina, and O. Hints (2011), Cryptospore assemblages from Upper Ordovician (Katian–Hirnantian) strata of Anticosti Island, Québec, Canada, and Estonia: Palaeophytogeographic and palaeoclimatic implications, *Rev. Palaeobot. Palynol.*, 166, 76–93.
- Walker, L. J., B. H. Wilkinson, and L. C. Ivany (2002), Continental drift and Phanerozoic carbonate accumulation in shallow-shelf and deep-marine settings, *J. Geol.*, 110(1), 75–87.
- Wallmann, K. (2003), Feedbacks between oceanic redox states and marine productivity: A model perspective focused on benthic phosphorus cycling, *Global Biogeochem. Cycles*, 17(3), 1084.
- Webby, B. D., F. Paris, M. L. Droser, and I. G. Percival (2004), *The Great Ordovician Biodiversification Event*, Critical moments and perspectives in Earth history and paleobiology, Columbia Univ. Press, New York.
- Winton, M. (2000), A reformulated three-layer sea ice model, *J. Atmos. Oceanic Technol.*, 17(4), 525–531.
- Yamanaka, Y., and E. Tajika (1997), Role of dissolved organic matter in the marine biogeochemical cycle: Studies using an ocean biogeochemical general circulation model, *Global Biogeochem. Cycles*, 11(4), 599–612.
- Yan, D., D. Chen, Q. Wang, J. Wang, and Z. Wang (2009), Carbon and sulfur isotopic anomalies across the Ordovician–Silurian boundary on the Yangtze Platform, South China, *Palaeogeogr. Palaeoclimatol. Palaeoecol.*, 274(1–2), 32–39.
- Young, S. A., M. R. Saltzman, W. I. Ausich, A. Desrochers, and D. Kaljo (2010), Did changes in atmospheric CO₂ coincide with latest Ordovician glacial–interglacial cycles?, *Palaeogeogr. Palaeoclimatol. Palaeoecol.*, 296(3–4), 376–388.
- Zhang, T., Y. Shen, R. Zhan, S. Shen, and X. Chen (2009), Large perturbations of the carbon and sulfur cycle associated with the Late Ordovician mass extinction in South China, *Geology*, 37(4), 299–302.
- Zhou, L., P. B. Wignall, J. Su, Q. Feng, S. Xie, L. Zhao, and J. Huang (2012), U/Mo ratios and $\delta^{98/95}\text{Mo}$ as local and global redox proxies during mass extinction events, *Chem. Geol.*, 324–325, 99–107.
- Zhuravlev, A. Y., and R. Riding (2001), *The Ecology of the Cambrian Radiation*, Critical moments in paleobiology and Earth history, Columbia Univ. Press, New York.